Continuum modeling of nodular cast iron using a porous plastic model with pressure-sensitive matrix— Experiments, model calibration & verification

Carl F O Dahlberg
Martin Öberg
Jonas Faleskog

KTH Royal Institute of Technology
School of Engineering Science
Department of Solid Mechanics
SE-100 44 Stockholm

February, 2014

Summary

Nodular cast iron from KBS-3 canister insert I53 has been investigated with respect to its plastic properties. Special interest was directed towards understanding the behavior under different states of stress triaxiality. Mechanical tests have been performed in compression, pure shear, uniaxial tension and two different notched tensile tests to sample the material in a range of triaxiality ranging from -1/3 to about 2/3. The tests clearly demonstrate that the material exhibits a so called strength differential (SD) effect where the yield stress in uniaxial compression is higher than in uniaxial tension. Moreover, the material contains a substantial amount of graphite nodules, which are treated as pre-existing voids. Classically this type of material is modeled by a Gurson-Tvergaard porous plasticity model with a yield surface that is symmetric with respect to the mean stress, i.e. without accounting for a SD-effect. In order to accurately describe the material a model that couples a porous aggregate description to a pressure sensitive matrix behavior has been used. All relevant parameters were determined from 3 of the 5 experiments and the 2 remaining sets were used to validate the model with good results.

Nodulärt gjutjärn från KBS-3 insats I53 har undersökts med avseende på dess plastiska egenskaper. Speciellt fokus har riktats mot att förstå beteendet vid olika spänningstillstånd, dvs olika treaxligheter. Mekanisk provning har utförts i kompression, ren skjuvning, enaxlig dragning och med två olika typer av notchade provstavar så att materialet har provats vid treaxligheter från -1/3 till ungefär 2/3. Testerna påvisade en klar skillnad i styrka då flytspänningen i enaxligt tryck är högre än i enaxligt drag. Materialet innehåller dessutom en relativt stor mängd grafitnoduler, vilka här behandlas som mikrohål. Vanligen så modelleras denna typ av material med en Gurson-Tvergaard modell för porös plasticitet som har en flytyta som är symmetrisk med avseende på det hydrostatiska spänningstillståndet, dvs den uppvisar ingen skillnad i styrka i drag mot tryck. För att beskriva detta material har en modell som kopplar samman en poröst plastisk beskrivning av aggregatet med en modell av ett tryckberoende matrismaterial använts. Alla relevanta materialparameterar har bestämts ur 3 av de 5 experimenten och de kvarstående 2 experimenten har använts för validering med goda resultat.

Nomenclature

	Quantity	Explanation
α	Matrix dilatancy	Pressure sensitivity factor, slope of matrix yield surface.
D_{ijkl}	Stiffness component	Fourth rank tensor. With superscript ep it denotes the tangent modulus.
δ_{ij}	Kronecker delta	Tensor; component is equal to 1 if $i = j$ and to 0 if $i \neq j$.
E	Young's modulus	Elastic stiffness parameter.
ε_{ij}	Component of strain	Total strain tensor. With superscript e or p for elastic or plastic strain.
ε^p	Equivalent plastic strain	Equivalent plastic strain, $\varepsilon^p = \int \dot{\varepsilon}^p \mathrm{d}t = \int \sqrt{\frac{2}{3}\dot{\varepsilon}_{ij}^p \dot{\varepsilon}_{ij}^p}\,\mathrm{d}t$.
$\bar{\varepsilon}$	Matrix equivalent strain	Equivalent deviatoric plastic strain in the matrix material.
f	Porosity	Void volume fraction
Φ	Yield function	$\Phi = \Phi\left(\sigma_{ij}, \bar{\sigma}, f\right)$
G	Shear modulus	Elastic stiffness parameter.
γ^p	Plastic shear strain	Shear component of plastic strain tensor.
I_1	First stress invariant	Trace of the stress tensor, $I_1 = \sigma_{kk} = 3\sigma_m$.
J_2	Second deviator invariant	Used to describe standard plasticity, $J_2 = \sigma_e^2 / 3$, i.e. Mises theory.
K	Bulk modulus	Elastic stiffness parameter.
ν	Poisson's ratio	Elastic lateral contraction parameter.
s_{ij}	Deviatoric stress component	Stress deviator tensor $s_{ij} = \sigma_{ij} - \sigma_m \delta_{ij}$.
σ_{ij}	Component of stress	Stress tensor.
σ_e	Effective stress	Magnitude of the stress state according to von Mises, $\sigma_e = \sqrt{\frac{3}{2} s_{ij} s_{ij}}$.
σ_m	Mean stress	Hydrostatic stress state, $\sigma_m = \frac{1}{3}\sigma_{kk} = \left(\sigma_{11} + \sigma_{22} + \sigma_{33}\right)/3$.
$\bar{\sigma}$	Matrix flow stress	Flow stress in the matrix material, $\bar{\sigma} = \bar{\sigma}\left(\bar{\varepsilon}\right)$, i.e. hardening relation.
T	Stress triaxiality	Ratio of mean stress to effective stress, $T = \sigma_m / \sigma_e$.
τ	Shear stress	Denotes a shear component of the stress tensor.
q_1	Porosity parameter	Constitutive parameter in the porous plasticity model.

Contents

1 Introduction

At the request of the Swedish Nuclear Fuel and Waste Management Company (SKB) the department of Solid Mechanics at KTH was tasked with investigating the plastic behavior of a nodular cast iron (NCI) from a canister insert. Previous mechanical tests performed on this material, see for instance Jenkins and Forrest (1990), has indicated that there is a difference in the yield point and post yield behavior between tensile and compression tests, thus hinting at a stress triaxiality dependence. It was concluded that a thorough study of the influence of stress triaxiality was needed and this is the main scope of this report. Further objectives, which are also covered in the report, were to investigate the variability of the mechanical properties, fracture behavior and fracture strain.

1.1 Background

Nodular cast iron is often thought of, and in engineering applications treated as, a standard metallic material, i.e. linear elastic with a standard J_2-flow (Mises) behavior or even a deformation plasticity description. This description is not very accurate for the plastic deformation since it fails to incorporate the known aspects of the microstructure. Due to the relatively high volume fraction of graphite particles NCI should be understood as a metal matrix particle composite. However, due to its macroscale homogeneity it can, by skillful application of homogenization techniques on the microscale, be treated as an isotropic and homogeneous continuum solid. The most commonly used constitutive description for this is the Gurson-Tvergaard (GT) model, see Gurson (1977) and Tvergaard (1981, 1982). This is a porous plasticity model where the graphite nodules are treated as preexisting voids, in a smeared out fashion, such that a homogeneous bulk material results. Examples of modeling of NCI using aforementioned model can be found in for instance Berdin et al. (2001), Brocks et al. (1996), Faleskog et al. (1998) and Steglich and Brocks (1997, 1998). The study by Benseddiq and Imad (2008) contains a good review of experiments on porous materials and modeling efforts with the GT-model and the related values reported for the constitutive parameters. Even though the original GT-model was constructed with a fairly low void volume fraction in mind, it has proven to be able to capture the behavior of aggregates with higher porosity as well, hence making it applicable to NCI, see for instance Brocks et al. (1996) where the volume fraction of voids is 11.4% and 12.0%.

Another equally useful modeling technique has been to construct a micromechanical representative model of the aggregate (i.e. bulk material + voids/particle inclusions) where the actual constituents are explicitly accounted for. The macroscopic mechanical behavior of such a model system can then be extracted by evaluation of the volume average tractions and displacements. Brocks et al. (1996) and Steglich and Brocks (1997, 1998) adopted an axisymmetric cylinder unit cell with one void in it to study void growth; this and similar models have also been used extensively to determine constitutive parameters for the GT-model, see for example the previously mentioned works and Faleskog et al. (1998) for a cell with a single void and Zhang et al. (1999) for parameter calibration using cells with multiple voids.

Several examinations of NCI with regards to microstructure evolution and micromechanical mechanisms of plastic deformation and subsequent failure exist in the literature. Thorough reviews on the subject can be found in Tvergaard (1990) and Benzerga and Leblond (2010), a scanning electron microscope (SEM) study of fracture surfaces and deformation mechanisms can be found in Martínez (2010) and a short but relevant introduction to some of the most mechanically and experimentally pertinent features of the NCI microstructure can be found in Ghahremaninezhad and Ravi-Chandar (2012). The most important finding regarding the graphite nodules in relation to mechanical loading is that the interface between the nodules and the surrounding ferrite matrix is very weak and will therefore debond at low loads. This

behavior justifies treating the graphite particles as voids since their mechanical interaction with the matrix becomes of limited importance. The shape and distribution of the nodules is of importance for the ductility as reported experimentally in Nilsson and Vokál (2009) and studied in conjunction with the GT-model in Brocks et al. (1996). Bonora and Ruggiero (2005) discuss the applicability of the assumption that the graphite is soft in relation to the ferrite by citing some evidence that several other allotropes of carbon (one of them being diamond) have been found to be present in NCI. However, they do not offer a conclusive statement regarding the possible influence of the graphite on the overall behavior. In order to fit the SD effect observed in the experiments they attempt to analyze, Bonora and Ruggiero (2005) introduces damage mechanism for the ferrite matrix in the micromechanical model they employ. For the work herein this is not taken into consideration and the nodules will be treated as voids.

The influence of the stress state on the initial yielding, subsequent void growth and failure have been studied previously in relation to the GT-model. A consequence of the shape of the yield surface is that the aggregate should yield at the same effective stress in tension and compression but at a higher value in shear, i.e. the yield surface is symmetric with respect to the stress triaxiality (the ratio of mean stress to effective stress, $T = \sigma_m / \sigma_e$). A dependence on triaxiality for the failure strain is well documented and examples can be found in Shi et al. (1992) for a NCI and in Bao and Wierzbicki (2004) on Al.

Interestingly another feature of the stress state dependence in NCI seems to be less appreciated. It has been observed that the yield point in compression is in fact not at all on the same level as in tension, but much closer to the yield point in shear, if not even higher. This would imply that the yield surface is in fact not at all symmetric with respect to the triaxiality and that there is a clear strength differential (SD) effect. This is for instance supported by material data from tests in compression and tension presented in the ASM Handbook (Jenkins and Forrest, 1990) as mentioned above. This report will introduce a porous plasticity description where this SD-effect has been taken into account by modeling the ferrite matrix as a pressure sensitive dilatant material. This SD-effect can be explained by a so called non-Schmid effects in materials with a body centered cubic (BCC) lattice and will be discussed in some detail later in this report.

1.2 Method

Since the objective of this study is to characterize the elastic-plastic behavior of the cast iron with regards to stress triaxiality five different mechanical tests, each with a distinct triaxiality value, have been performed. In addition to the mechanical tests a microstructure analysis has been performed and fractures surfaces have been investigated in a scanning electron microscope (SEM) to provide an understanding of the aggregate material composition. The results of the mechanical tests and the microstructure analysis are used to develop a continuum mechanical model and determine the relevant parameter values. A subset of the mechanical tests will not be used in the model development, but instead used for validation purposes to see if the model can predict the behavior of these.

2 Experiments

This section details the material characterization with microstructure analysis and mechanical testing.

2.1 Material

The material investigated is a nodular cast iron, and is taken from a canister insert BWR I53, a test casting done by SKB. Specifically, it is taken 2850 mm above the bottom in the axial direction of the channels and 94° from the zero-meridian in relation to the non-destructive testing. It was delivered to KTH cut in the shape of approximately square bars (32×32×160 mm^3). In Figure 2-1 the material is shown prior to being cut into square bars. The material can best be described as an aggregate material consisting of an iron-ferrite matrix interspersed with spherical, or close to spherical, graphite nodules.

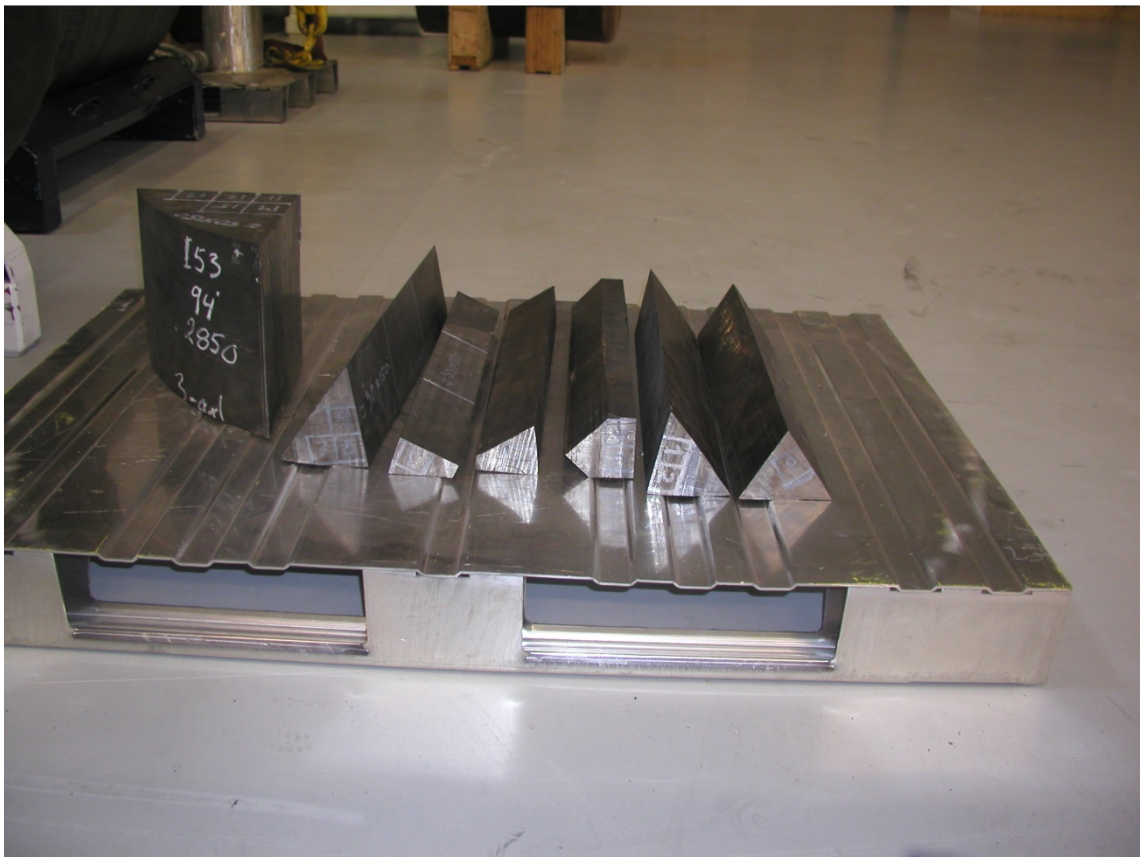

Figure 2-1. Test material prior to cutting and delivery to KTH.

Several reports on the microstructure of this material have already been produced and can be found in “Materialprovning av segjärnsinsats I53” (SKBdoc 1094762), “Materialprovning av segjärnsinsats I53 (Mitten/Botten)” (SKBdoc 1206724) and “Strukturundersökning vidgjutna ämnen I53-I57” (SKBdoc 1414396). The former two reports (from 2007) lacked a crucial, for the work intended herein, piece of information – the volume fraction of graphite nodules. In the latter report (from 2013) a metallographic investigation of the cast-on samples from I53-I57 is presented with reported values of 12.0% to 12.5% for the volume fraction. However, since cast-on samples may not be entirely representative of the bulk material in the insert, an estimate based on image analysis using of the microstructures in “Materialprovning av segjärnsinsats

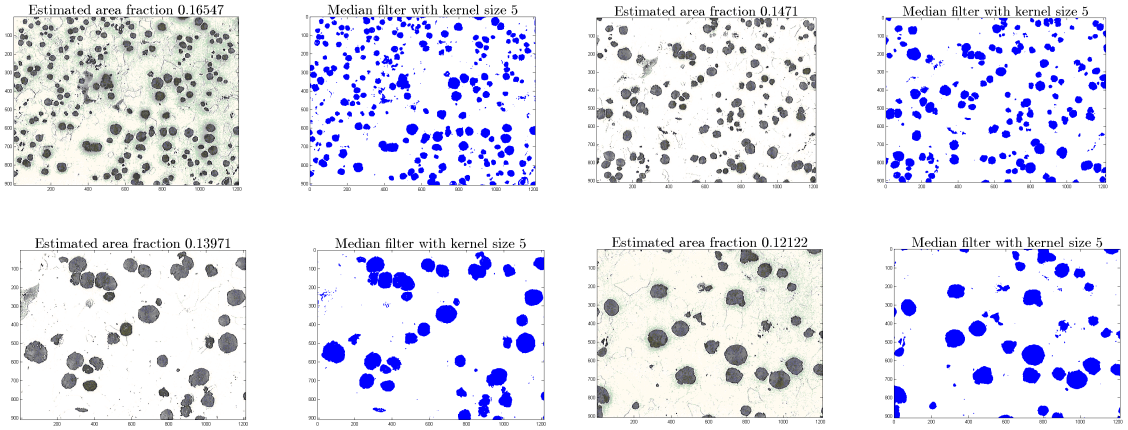

Figure 2-2. Microstructure images from the SweCast report on specimens taken from the middle of canister insert I53 and the corresponding median filtered images used for volume fraction estimation.

I53” (SKBdoc 1094762) was conducted which yielded results varying from 12.1% to 16.5% based on median filtered monochrome images and a simple pixel count, see Figure 2-2.

Due to the large spread in values for the volume fraction from the simple image analysis and the importance of getting a reliable estimate, the microstructure was also analyzed by Peter Hedström at KTH Materials Science. Three samples were considered, one from each of the un-deformed parts of the tensile test specimens 17254, 17256 and 17258. The results, shown in Table 2-1, indicate an average area fraction of graphite of about 12.5% and since the graphite nodules essentially are spherical this can be directly translated to a volume fraction, see for instance Friel et al. (2000). Examples of the microstructure from this study are shown in Figure 2-3. The fraction of perlite was also estimated and was found to be low, between 0.5-2%. In addition, several images from this study were analyzed by the same method used above on the images from “Materialprovning av segjärnsinsats I53” (SKBdoc 1094762) and the results were in good agreement with the average results in Table 2-1. The right picture in Figure 2-3, roughly covering a quarter of the cross-section of the 10 mm diameter head of a specimen (not subjected to any load), display another important feature of the microstructure: the graphite nodules are not evenly distributed in the cast iron. Furthermore, the graphite nodules vary in size, in addition to the spatial variation. This feature of the microstructure will not significantly affect the overall elastic-plastic response of the cast iron, but will have a significant effect on the failure strain, as will be evident from the test results to be presented below.

	17254	17256	17258
Area fraction graphite [%]	14.80	11.56	12.13
	14.04	13.07	13.16
	11.00	12.70	8.60
Average	13.28	12.45	11.27
Standard deviation	2.01	0.79	2.41
Area fraction Perlite [%]	2.04	0.44	1.10

Table 2-1. Results from the microstructure analysis.

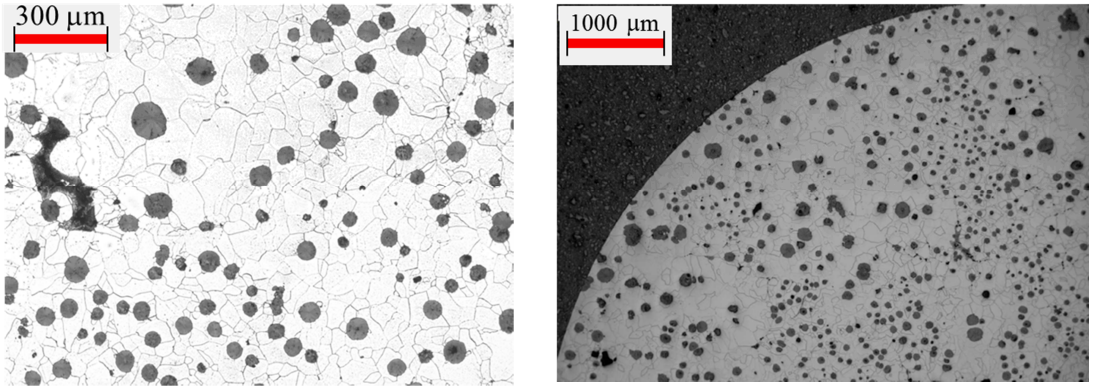

Figure 2-3. Examples of the microstructure from the analysis by Peter Hedström, KTH Materialvetenskap.

2.2 Specimen geometry and experimental setup

Tests were carried out on five different types of specimen geometries. A cylindrical specimen tested in uniaxial compression, a tube specimen with thin gauge section tested in pure shear, a standard smooth round bar specimen tested in uniaxial tension, and two types of round bar specimens with axisymmetric notches—one with a smooth notch and one with a sharper notch. Together these tests cover the range from -1/3 to about 2/3 in stress triaxiality. The tests and specimens used will be presented in some detail next.

2.2.1 Uniaxial test in tension on smooth round bar specimens

Tensile tests were performed on smooth cylindrical dog-bone specimens with two different diameters in order to determine the Young's modulus, the 0.2% offset yield stress, post yield behavior and the failure load. For the first series of tensile tests, 6 specimens with a nominal diameter of 5 mm and length 32 mm were manufactured pairwise from three of the square bar pieces selected at random. The specimens were numbered 17254 to 17259, where the first two come from the same square bar, the next two from a second bar and finally the last two from yet a another bar. Later, material from the same bars was used to construct the first series of notched specimens.

A second series of smooth specimen tensile tests were performed on specimens with a larger cross sectional area to account for statistical effects of graphite nodule distribution. For this test series another set of 6 specimens were manufactured with a diameter of 9 mm and given the designation 17345-17350. Specimen number 17345 was tested at liquid nitrogen temperature to ensure a brittle fracture surface. Special care was taken with all tests in this series to protect the fracture surfaces from damage to enable a SEM study of the surfaces.

2.2.2 Tests in tension at elevated triaxiality on notched round bar specimens

Two sets of notched tensile tests have been performed with the aim of raising the triaxiality above 1/3, i.e. higher than for a uniaxial tensile test. These tests were done to be able to evaluate the predictive capabilities of the continuum model outside the range of triaxiality where the model parameters will be fitted to the experiments. The schematic geometry of the notched specimens is shown in Figure 2-4. The specimens 17271 to 17276 had a large notch radius $r = 15$ mm, and specimens 17280-17285 had a sharper notch with $r = 3.75$ mm. Bridgman's estimate of the average stress triaxiality is

$$T = \frac{1}{3} + \ln\left(1 + \frac{R}{2r}\right), \qquad (1)$$

where $R = 3$ mm is the radius of the notch root, and gives $T = 0.43$ and $T = 0.67$ respectively in these two cases.

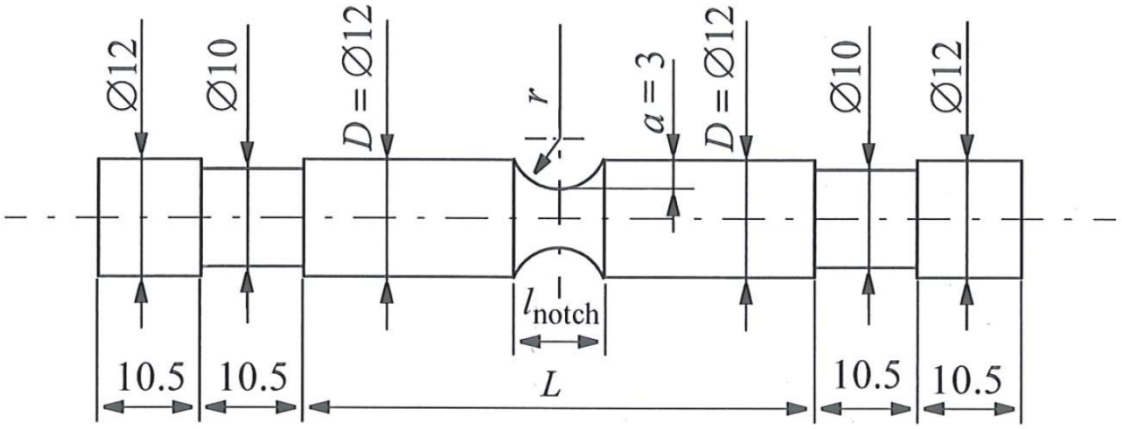

Figure 2-4. Schematic illustration of the notched tensile test specimen geometry.

2.2.3 Uniaxial test in compression on short cylindrical specimens

Compression tests were performed on cylindrical specimens compressed between two plates of high strength steel. The experimental setup was calibrated by compressing the two steel plates without the specimen and the compliance of the setup was determined and later accounted for in the piston movement data. Two strain gauges were glued to opposing sides to closely monitor the deformation in the first part of the test (1-4%) and after the strain gauges failed the piston movement was used to measure the deformation. The piston displacement signal was calibrated so that it corresponded to the strain gauge measures in that region. Initial compression tests with lubricated contact surfaces exhibited a barreling effect due to contact friction. To reduce the friction 6 circular grooves were machined on the surface. The grooves were filled with lubricant, and as a specimen was compressed the lubricant would be expelled out of the grooves and onto the surface continuously, thus keeping the contact surface well lubricated throughout the entire test. This significantly reduced the barreling, even at large compressive strains (~30%). Figure 2-5 shows the specimen where the diameter $D = 10$ mm, height $H = 10$ mm, depth of the grooves $h = 0.1$ mm and the tip radius of the grooves $R = 10$ µm. A specimen subjected to a compressive strain of about 30% is also shown to the left in Figure 2-5, with its un-deformed shape indicated by the dashed line. Note that there is virtually no barreling visible. See Table 2-2 for actual measured values of the geometry for each specimen. The lubricant used was molybdenum disulfide.

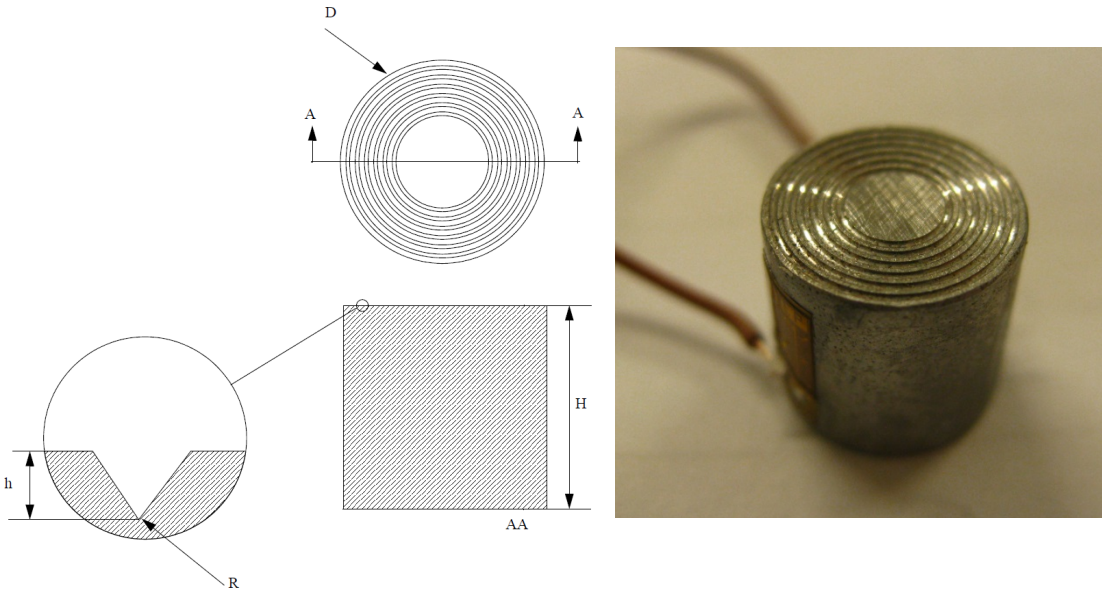

Figure 2-5. (Left) The geometry of a compression test specimen with triangular shaped grooves for lubricant. (Right) Picture of a compression specimen with strain gauge.

Shear tests were performed by torsion of cylindrical specimens with a thin-walled section intended to contain almost all plastic deformation. The size and corner radius of the thin-walled section was chosen by a FE-design of experiment to minimize plastic deformation outside the region and to make sure that the shear stress acting on the cross section could be found from the applied torque. Aluminium blocks were attached above and below the test region with steel strips extending from them forming a gap that would open as torque were applied. The opening displacement was measured by a clip gauge. See Figure 2-6 for details on the geometry of the test specimen and a picture of the experimental setup. Four specimens, numbered 17299 and 17306-17308, were manufactured and tested. The fracture surface of specimen 17306 was also analyzed by SEM imaging.

The twist angle θ of the specimen during the test can be calculated from the geometry of the setup and the clip gauge opening displacement δ

$$\theta = 2\arcsin\left(\frac{\delta + d_0}{2R_c}\right) - 2\arcsin\left(\frac{d_0}{2R_c}\right), \qquad (2)$$

where d_0 is the initial opening of the clip gauge and R_c is the distance from the cylinder axis to the edge of the clip gauge. Engineering shear strain is given as

$$\gamma = \theta \frac{R_m}{h}, \qquad (3)$$

where R_m is the mean radius of the thin-walled section and $h = 4.03$ mm is the height of the thin-walled part, see Table 2-3 for details on the geometry of each specific test specimen. The shear stress over the cross section is calculated from the applied torsional moment M as

$$\tau = \frac{M}{2\pi R_m^2 t}, \qquad (4)$$

where t is the thickness of the thin-walled part.

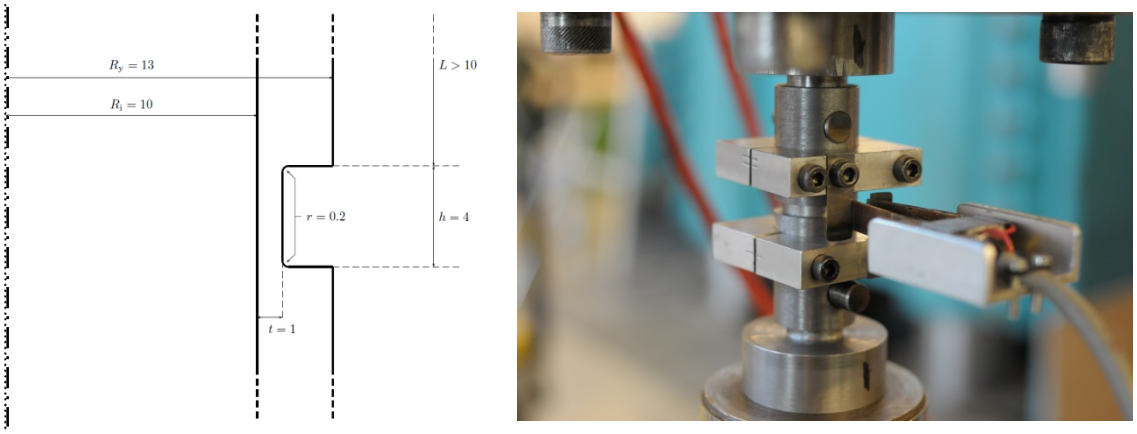

Figure 2-6. (Left) Schematic of the thin-walled section geometry. (Right) Picture of the experimental setup showing a specimen mounted in the fixtures and aluminium blocks with a clip gauge attached.

2.2.4 General aspects of tests

All tests were post-processed in the same general fashion. A smoothing operation was applied to each individual specimen curve in order to filter out the experimental noise – first a robust Lowess quadratic fit and then a moving average. For the tension and compression experiments the stress and strain data was converted from engineering quantities ($\sigma_{eng}, \varepsilon_{eng}$) to the corresponding true values ($\sigma_{true}, \varepsilon_{true}$) according to

$$\begin{aligned} \varepsilon_{true} &= \ln\left(1+\varepsilon_{eng}\right) \\ \sigma_{true} &= \sigma_{eng}\left(1+\varepsilon_{eng}\right) \end{aligned} \qquad (5)$$

It should here be emphasized that in this case equation (5) is only an approximation due to the expected plastic dilatational behavior of the aggregate. Plastic strains were calculated by determination of the initial elastic slope and subtracting the elastic strains. To extract a *master curve* from each set of experiments all individual curves in each set was interpolated to the same set of strain values and the average over the set was taken as the master stress value for that strain point.

The tensile and compression tests were performed in a MTS 100 kN rig and the torsion tests in a MTS 160 kN/1.1 kNm rig. The 100 kN load cell is class 1 which means it has an accuracy of within 1%, a repeatability of 1%, is reversible within 1.5%, with a zero-error less than 0.1% and a resolution within 0.5%. The moment load cell MTS 288 kNm was also rated at class 1 at the load inspection. The extensometers used were Instron 2620-602 with accuracy within 1% and the clip gauge used was an MTS 12.5 mm calibrated to an accuracy of 1% within the elastic and initial plastic range and then has an accuracy of about 2% further into the plastic region. The dimensions of all specimens were measured with a tolerance of +/- 0.01 mm.

2.3 Experimental results

In Figure 2-7 the experimental results for tension, pure shear and compression are shown in the form of one curve for each setup; henceforth called master curves—the average behavior of each test series. The experimental results showed a clear difference in initial values of the von Mises effective stress at the yield point as shown in Figure 2-7 where the master curves in terms of effective stress vs. equivalent plastic strain of the experiments are plotted. For the tension and compression experiments this is straight forward to plot, but for the shear the effective stress is calculated as $\sigma_e = \sqrt{3}\tau$ and the equivalent strain as $\varepsilon_e^p = \gamma^p / \sqrt{3}$. The yield point in tension, 269 MPa, is markedly lower than those for the compression and shear experiments which seem

to yield at about the same value, ~290 MPa. It can also be seen that the material hardens more in compression than in tension which is expected of a material with voids that grow in tension and shrink in compression.

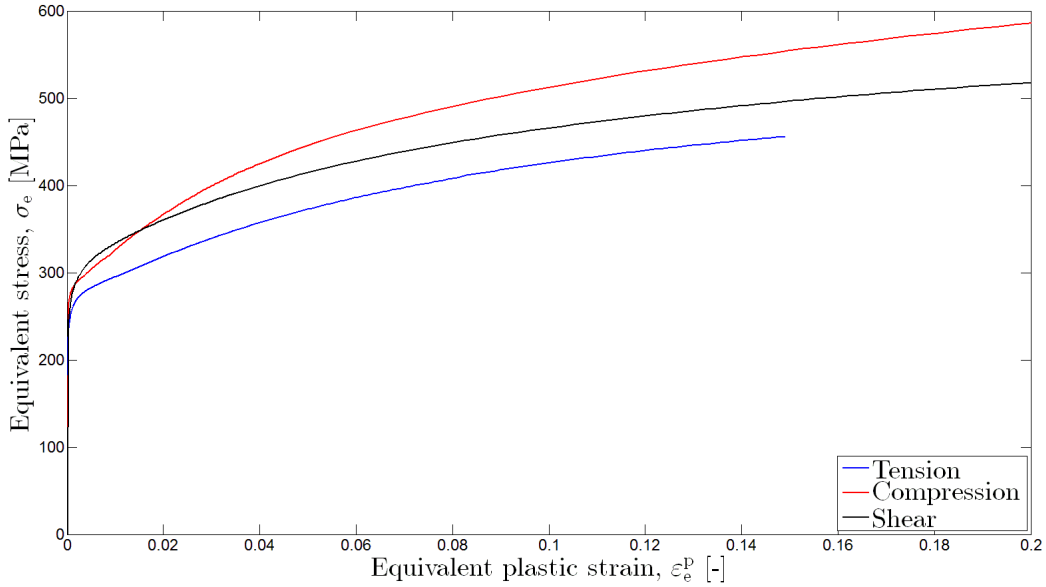

Figure 2-7. Summary of tension, compression and shear experiments.

2.3.1 Uniaxial test in compression—Results

Six compression tests were performed according to the experimental setup described above. Individual specimen geometries are listed in Table 2-2 below. The specimens were numbered 17300 to 17305 and the post-processed results plotted together with the master curve can be seen in Figure 2-8. In Figure 2-9, one of the short cylindrical specimens is shown after a test that was interrupted when a compressive strain of about 0.3 had been reached. The un-deformed shape is indicated by the dashed white line. It can be observed that the barreling, that does in fact exists, is so small that it cannot be distinguished on the scale of the picture.

Specimen	D / mm	H / mm	$R_{p0.2\%}$ / MPa
17300	10.02	10.04	292
17301	10.03	10.07	290
17302	10.02	10.04	291
17303	10.01	9.91	290
17304	10.03	10.04	281
17305	10.03	10.03	290

Table 2-2. Compression test specimen geometries.

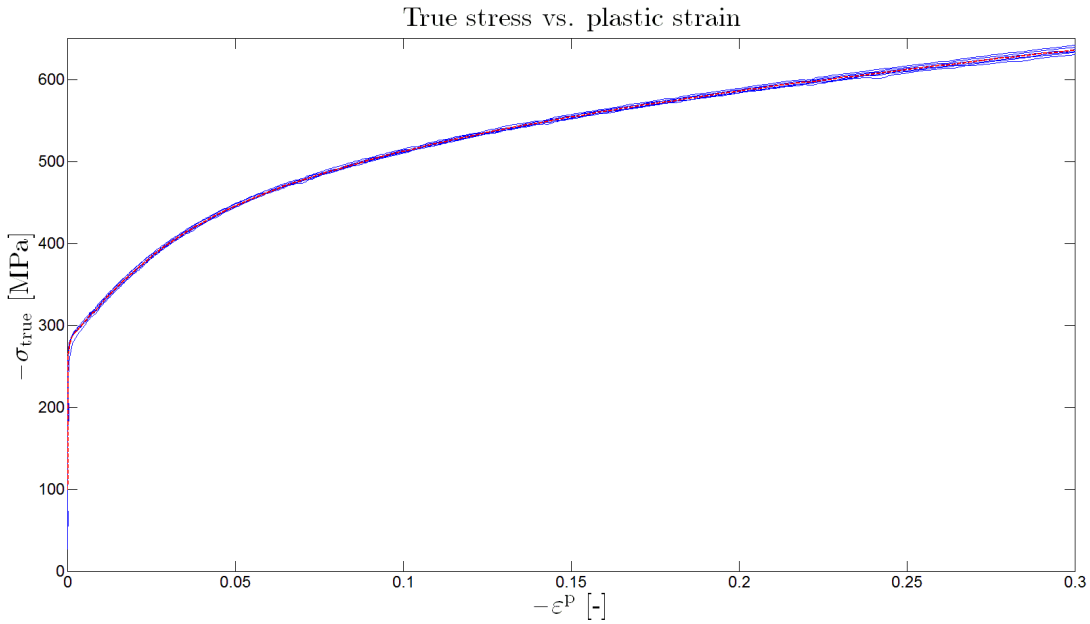

Figure 2-8. Compression test results in solid blue lines with master curve represented by a dashed red line.

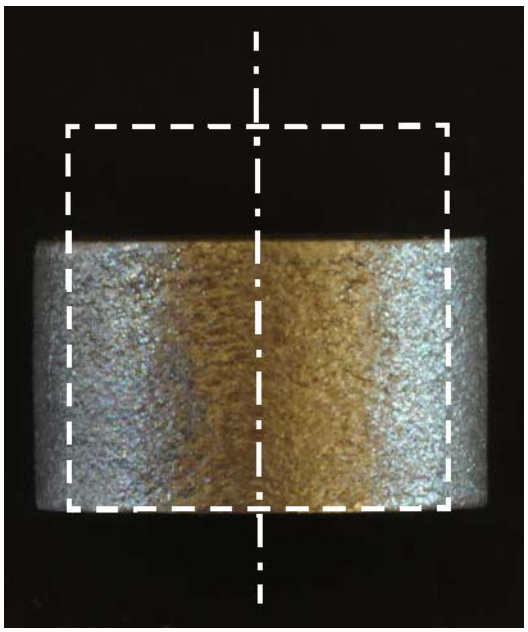

Figure 2-9. Deformed specimen 17305 with undeformed shape indicated by the white dashed lines.

2.3.2 Torsion test in pure shear—Results

Four torsion tests were performed and evaluated according to the setup detailed above. The specimen geometries were measured and are detailed in Table 2-3 below. The height of the thin-walled section, $h = 4.03$ mm, was exactly the same in each test since it was machined by the same tool-bit. The specimens were numbered 17299 and 17306-17308 and the post-processed results plotted together with the master curve (Figure 2-7) are shown in Figure 2-10.

Specimen	R_i / mm	R_v / mm	R_m / mm	d_0 / mm	t / mm	$R_{p0.2\%}$ / MPa
17299	10.04	11.02	10.53	3.5	0.99	286
17306	10.03	11.00	10.52	4.1	0.97	290
17307	10.04	11.00	10.52	3.9	0.96	296
17308	10.04	10.99	10.51	3.6	0.96	294

Table 2-3. Geometry of cylindrical torsion test specimens.

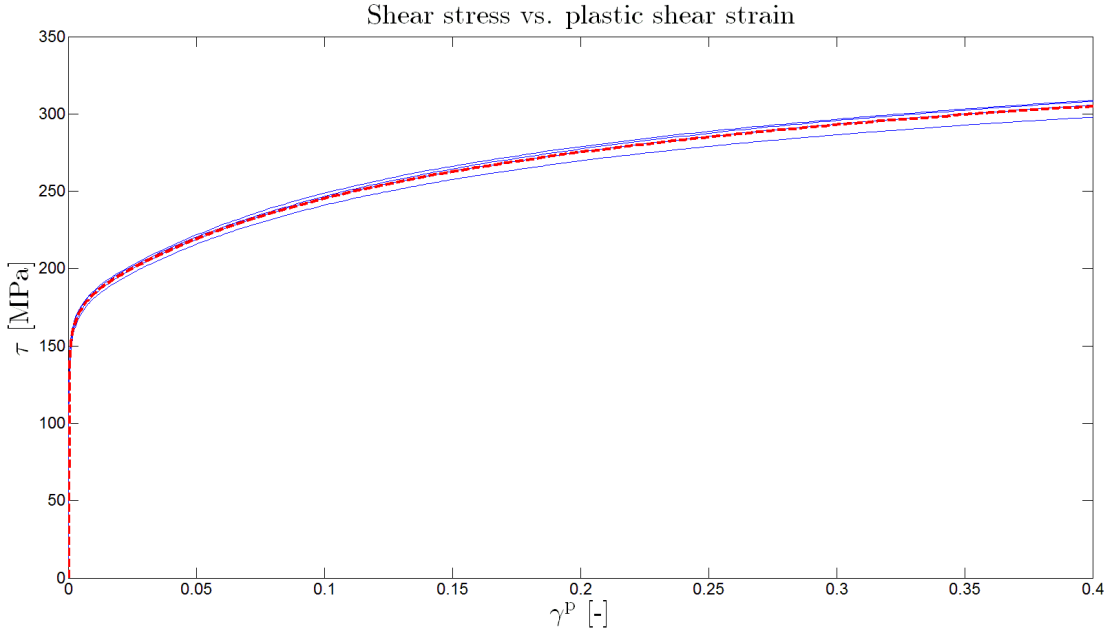

Figure 2-10. Shear test results in blue solid lines and master curve in dashed red. Shear stress in thin-walled part vs. plastic shear strain.

2.3.3 Uniaxial test in tension—Results

The experimental engineering stress vs. engineering strain curves (raw data) are shown in Figure 2-11. The red curves are from the smaller diameter experiments and the blue curves are from the larger diameter specimens. The un-processed data is shown because it clearly illustrates that there is very little scatter in the elastic and initial plastic properties, but there is a large difference in fracture strain (0.04-0.2) due to local variations in the concentration of graphite nodules as well as the existence of various defects. If a gauge section of a specimen contains a significant volume of a higher than average concentration of nodules, a lower strain to fracture can be expected. However, it may be interesting to note that once the onset of failure has occurred, it progress in a rather stable manner until virtually all load carrying capacity is gone. With a few exceptions, this failure process appears to be fairly repetitive and consistent, and seems to occur over an increment in strain of about 0.01. Summaries of the two sets of tests are given in Table 2-4 and Table 2-5. There was no perceivable amount of necking observed before fracture occurred.

Since the second set extends further in strain values it has been used to determine the *master curve* for the uniaxial tension load case. In Figure 2-12 the true stress vs. logarithmic plastic strain is plotted for specimen 17346-17350 and the resulting master curve is overlaid in red.

Specimen	E-modulus / GPa	$R_{p0.2\%}$ / MPa	R_m / MPa	Diameter / mm
17254	168	270	371	4.97
17255	167	270	376	4.96
17256	166	270	374	4.97
17257	167	269	328	4.96
17258	167	270	390	4.96
17259	167	266	389	4.95

Table 2-4. Tensile test results for smooth specimen with initial cross section area of ~19mm^2 . Specimen 17257 has a significantly lower R_m due to a large casting pore which caused an early fracture.

Specimen	E-modulus / GPa	$R_{p0.2\%}$ / MPa	R_m / MPa	Diameter / mm	Temperature
17345	-	-	470	9.09	Liquid N
17346	167	267	380	9.02	RT
17347	168	266	392	9.08	RT
17348	166	267	375	9.10	RT
17349	167	271	392	9.12	RT
17350	168	269	395	9.09	RT

Table 2-5. Tensile test results for smooth specimen with initial cross section area of ~64mm^2. Specimen 17345 was immersed in liquid nitrogen and was consequently not equipped with a clip gauge, hence only the peak engineering stress (R_m) could reliably be measured. The other tests were carried out at room temperature (RT).

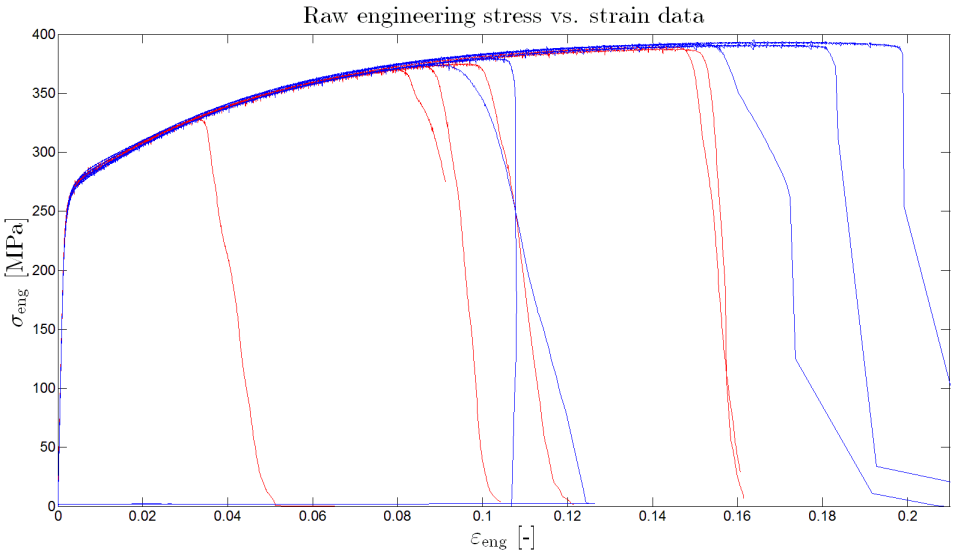

Figure 2-11. Engineering stress-strain data from both sets of uniaxial tensile tests. Red curves correspond to specimen 17254-17259 (smaller diameter) and blue curves to specimen 17346-17350.

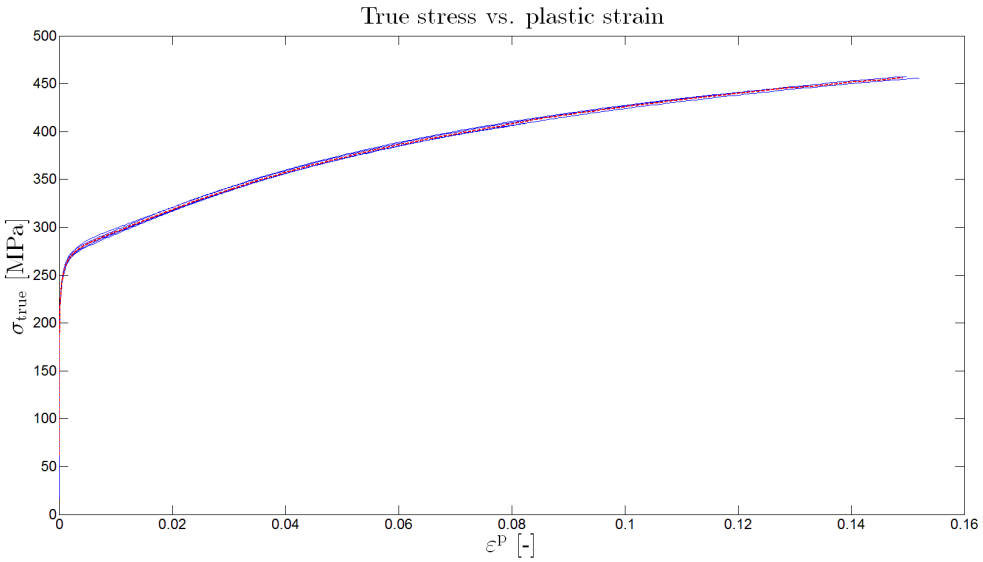

Figure 2-12. True stress vs. (logarithmic) plastic strain for specimens 17346-17350 (blue solid lines) and the resulting master curve (red dashed line).

2.3.4 Tests on notched round bar specimens—Results

The nominal stress in the notch root (applied force divided by initial cross section area) versus normalized gauge length elongation is plotted for both sets of notched tensile tests in Figure 2-13. The specimens are listed in Table 2-6. In Figure 2-13 the curve for specimen 17284 is excluded because it was probably accidentally torqued before being mounted in the test fixture and was therefore exposed to an uncontrolled amount of deformation hardening prior to the test. In Figure 2-13, the blue lines pertain to specimens with the smooth notch and the red lines represent the specimens with a sharp notch. Again, note that prior to the onset of failure, all curves give a fairly consistent and collective view of the plastic response. However, the onset of failure exhibit a significant scatter as also observed in the tests on smooth round bar specimens.

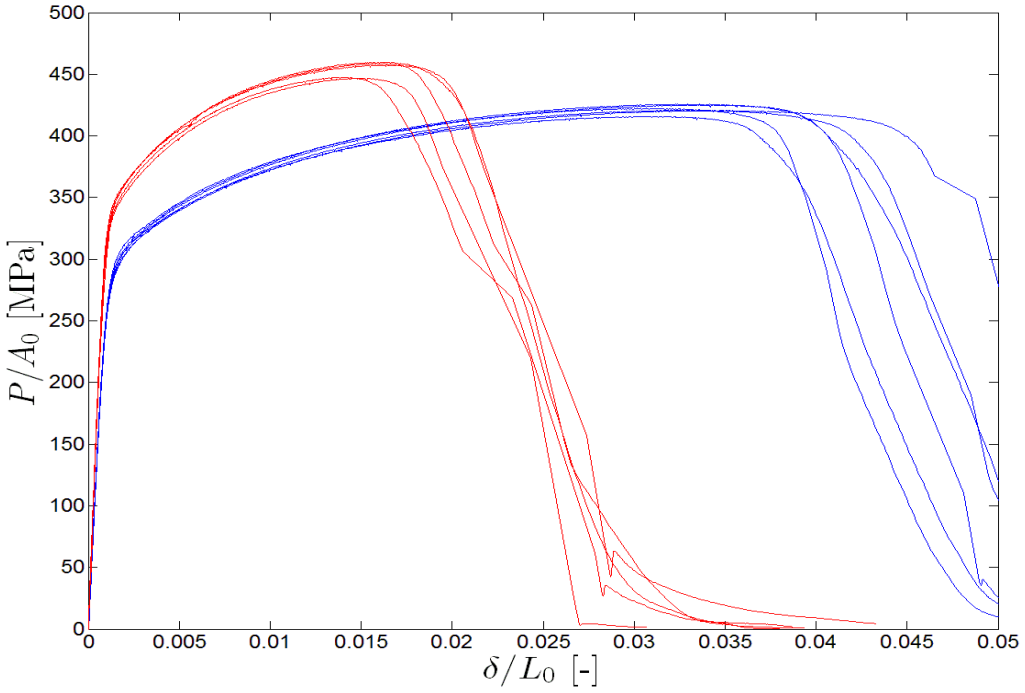

Figure 2-13. Notched tensile test results. Blue curves are for $r = 15$ ***mm and red curves are for*** $r = 3.75$ ***mm. Horizontal axis gives values of elongation divided by gauge length and vertical axis gives applied force over initial cross section area at the notch root.***

Specimen	Diameter / mm	Comment
17271	5.98	Notch with $r = 15$ mm. From same square bar as 17254-5
17272	6.01	Notch with $r = 15$ mm. From same square bar as 17254-5
17273	5.96	Notch with $r = 15$ mm. From same square bar as 17256-7
17274	5.99	Notch with $r = 15$ mm. From same square bar as 17256-7
17275	6.01	Notch with $r = 15$ mm. From same square bar as 17258-9
17276	5.98	Notch with $r = 15$ mm. From same square bar as 17258-9
17280	5.99	Notch with $r = 3.75$ mm.
17281	5.99	Notch with $r = 3.75$ mm.
17282	5.97	Notch with $r = 3.75$ mm.
17283	5.98	Notch with $r = 3.75$ mm.
17284	6.03	Notch with $r = 3.75$ mm. Excluded, see text.
17285	5.99	Notch with $r = 3.75$ mm.

Table 2-6. Notched tensile test specimens.

3 Constitutive model and parameter estimation

The microstructure of the material and the experimental results reveal two important features the material model need to capture. Those are (*i*) the microstructure contains a substantial amount of graphite nodules that are assumed be loosely bonded to the ferrite matrix, and are here treated as pre-existing voids; (*ii*) the uniaxial tests in compression and in tension display a very clear strength differential effect (SD), and this SD-effect can only be attributed to the matrix material. A material model that accounts for these features is recently proposed by Guo et al. (2008). This model will be employed here and henceforth referred to as the GFS-model (Guo/Faleskog/Shih-model). The GFS-model is a plasticity model for a porous solid with a pressure-sensitive dilatant matrix material. The matrix is modeled as a Drucker-Prager material with a yield criterion that depends on the first stress invariant I_1 ($=3\bar{\sigma}_m$, with $\bar{\sigma}_m$ being the mean stress) and the second deviatoric stress invariant J_2 ($=\bar{\sigma}_e^2/3$, with $\bar{\sigma}_e$ being the effective stress), defined as

$$\bar{\sigma}_e + 3\alpha\bar{\sigma}_m = \bar{\sigma}\left(\bar{\varepsilon}\right) \qquad (6)$$

Here, α is a pressure sensitive factor that defines the SD-effect, and $\bar{\sigma}(\bar{\varepsilon})$ is the current flow stress of the material under pure shear, which depends on the deviatoric equivalent plastic strain $\bar{\varepsilon}$. Based on an upper bound analysis, which utilizes a Gurson type of homogenization to derive a yield function and an associated flow rule, Guo et al. (2008) propose an approximate yield function that for matrix materials exhibiting a limited influence on I_1, as in the present application, is very accurate. In a very recent independent examination of porous pressure-sensitive materials in general, Pastor et al. (2013) conclude that the GFS-model is an appropriate choice for structural computations made of the porous Drucker-Prager material.

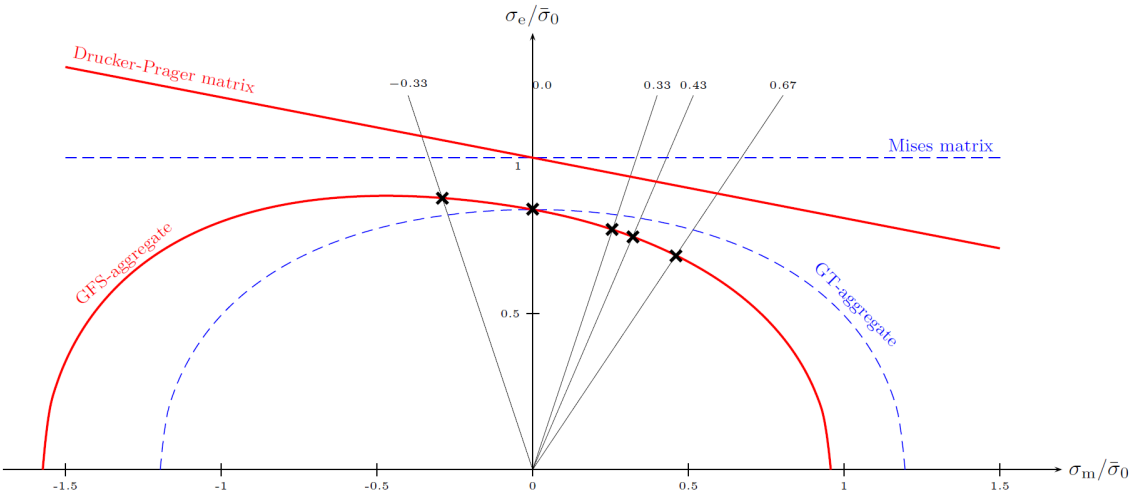

Figure 3-1. Illustration of the yield surface for the Guo-Faleskog-Shih porous solid with a pressure-sensitive matrix of Drucker-Prager type (red solid curves). The unsymmetrical shape of the aggregate yield surface is required to capture the experimental data (represented by black crosses). The Gurson-Tvergaard porous aggregate with a Mises matrix (blue dashed lines) is included for comparison. Lines of constant triaxiality are shown, corresponding to the average triaxiality of the experiments.

The key features of the yield function are shown in Figure 3-1. The red line marked "Drucker-Prager matrix" illustrates the yield behavior of the matrix material. The red curve marked "GFS-aggregate displays the yield surface of the porous solid, which clearly indicates the strong influence of the relatively large void volume content on macroscopic behavior. The blue dashed curves pertain to the Gurson model, where the matrix material is described as a Mises material, which is included for comparison purposes. The solid straight lines indicate the stress states in the five different types of experiments that have been carried out. The black cross markings on

these lines represents where the onset of plastic yielding occurred in these experiments. Note that the Gurson-Tvergaard model significantly would overestimate the flow stress for positive mean stresses. Thus, it is evident from the experimental results that the Gurson-Tvergaard model does not capture all the pertinent features of the nodular cast iron, as the GFS-model seems to do.

The physical explanation for an I_1 influence on the matrix material may be attributed to a non-Schmid effect, and is typically seen in metals with a body centered cubic (BCC) lattice, as in ferrite. In such metals plastic slip is largely due to screw dislocations and these give rise to non-symmetric and non-planar slip, which is the main cause of the non-Schmid effects, see Vitek et al. (2004) and Dao et al. (1996). In BCC-polycrystals this can give rise to a significant SD-effect as shown by these authors as well as in Chen et al. (2013). For instance calculations made by Tjahjanto (2008, page 30) for a polycrystalline system of ferrite (75%) and bainite (25%), using a Taylor average, gives an SD-effect quantified as $(\bar{\sigma}_c - \bar{\sigma}_t)/\left[(\bar{\sigma}_c + \bar{\sigma}_t)/2\right] \approx 0.06$, where $\bar{\sigma}_c$ and $\bar{\sigma}_t$ represents the initial yield stress in compression and tension, respectively. This is in fact very close to what is found here for the ferrite/perlite matrix of the nodular cast iron, as will be shown below.

3.1 Incremental constitutive equations of the GFS-model

The model is based on the framework of rate independent incremental plasticity accounting for finite strains. In the following a superscript dot, e.g. $\dot{x}$, denote rates and the Einstein tensor notation will be used. The kinematic relations are phrased in terms of an additive decomposition of spatial rate of deformation tensor as

$$\dot{\varepsilon}_{ij} = \dot{\varepsilon}^e_{ij} + \dot{\varepsilon}^p_{ij} \,. \qquad (7)$$

Note that in (7), $\dot{\varepsilon}_{ij}$ is identical to the small strain rate tensor in case of infinitesimal deformations. The elastic behavior is governed by standard linear elasticity, here given on rate form

$$\overset{\nabla}{\sigma}_{ij} = D_{ijkl}\left(\dot{\varepsilon}_{kl} - \dot{\varepsilon}^p_{kl}\right), \qquad (8)$$

where $\overset{\nabla}{\sigma}_{ij}$ is an objective rate of the Cauchy stress tensor (the Jaumann rate is employed in Abaqus) and the elastic stiffness tensor can be formulated in terms of Young's modulus E, Poisson's ratio ν and the Kronecker delta δ_{ij} as

$$D_{ijkl} = \frac{E}{1+\nu}\left[\frac{1}{2}\left(\delta_{ik}\delta_{jl} + \delta_{il}\delta_{jk}\right) + \frac{\nu}{1-2\nu}\delta_{ij}\delta_{kl}\right]. \qquad (9)$$

Note that the elastic stiffness relation refers to the initial conditions of the aggregate, and is assumed to remain constant during the evolution of porosity. Plastic yielding is controlled by the yield criterion

$$\Phi\left(\sigma_{ij}, \bar{\sigma}, f\right) = \begin{cases} < 0, & \text{elastic} \\ = 0, & \text{plastic} \end{cases} \qquad (10)$$

The GFS-model yield function is given in terms of the effective stress σ_e and mean stress σ_m of the porous solid aggregate by

$$\Phi = \left(\frac{\sigma_e}{\Theta}\right)^2 + 2q_1 f \cosh\left[\gamma^{-1}\ln\left(1 - \frac{3q_2\alpha\sigma_m}{\bar{\sigma}}\right)\right] - \left(1 + \left(q_1 f\right)^2\right) = 0 \qquad (11)$$

where

$$\Theta = \bar{\sigma} - \frac{3\alpha\sigma_m}{\left(1 - q_1 f\right)^{1/2 - \alpha\,\mathrm{sgn}\,\sigma_m}}, \qquad \gamma = \frac{2\alpha}{2\alpha + \mathrm{sgn}\,\sigma_m}. \qquad (12)$$

Here, α is the pressure sensitive factor of the matrix material discussed above. The current state is characterized by the void volume fraction *f*, and the flow stress $\bar{\sigma}$ of the undamaged matrix material under pure shear, as discussed above. A small modification of the original GFS-model is introduced here, and that is the introduction of the parameters q_1 and q_2, in much the same manner as introduced by Tvergaard (1981, 1982) for the Gurson model.

Normality gives an associated flow rule as

$$\dot{\varepsilon}_{ij}^{p} = \dot{\lambda}\frac{\partial \Phi}{\partial \sigma_{ij}} = \frac{1}{H}\frac{\partial \Phi}{\partial \sigma_{ij}}\frac{\partial \Phi}{\partial \sigma_{kl}}\dot{\sigma}_{kl} \qquad (13)$$

with $\dot{\lambda}$ being a plastic multiplier defined by the consistency condition. For the choice of stress rate in (13) see a discussion in Needleman (1985). The generalized plastic modulus is

$$H = -\left[\left(\frac{h}{1-f}\frac{\partial \Phi}{\partial \bar{\sigma}} - 3\alpha\frac{\partial \Phi}{\partial f}\right)\frac{1}{\bar{\sigma}}\sigma_{ij}\frac{\partial \Phi}{\partial \sigma_{ij}} + \frac{\partial \Phi}{\partial f}(1-f)\frac{\partial \Phi}{\partial \sigma_{m}}\right], \qquad (14)$$

where $h = \dot{\bar{\sigma}} / \dot{\bar{\varepsilon}}$ is the slope of the matrix flow stress versus deviatoric effective plastic strain curve. As the material model contains two internal state variables, i.e. *f* and $\bar{\sigma}$, evolution equations need to be specified for those. For the void volume fraction, *f*, two contributions must be accounted for, volume changes due to porosity and in the matrix. The latter being a consequence of the Drucker-Prager response of the matrix. If also the elastic dilation is neglected, the evolution law for the void volume fraction may be written as

$$\dot{f} = (1-f)\left(\dot{\varepsilon}_{kk}^{p} - 3\alpha\dot{\bar{\varepsilon}}\right) = \left((1-f)\frac{\partial \Phi}{\partial \sigma_{m}} - \frac{3\alpha}{\bar{\sigma}}\sigma_{ij}\frac{\partial \Phi}{\partial \sigma_{ij}}\right)\dot{\lambda}\,. \qquad (15)$$

The evolution law for the matrix flow stress can alternatively be phrased in terms of the equivalent plastic strain that results from the equivalence of the plastic work rate between matrix and the aggregate as

$$\dot{\bar{\varepsilon}} = \frac{\sigma_{ij}\dot{\varepsilon}_{ij}^{p}}{(1-f)\bar{\sigma}} = \frac{1}{(1-f)\bar{\sigma}}\sigma_{ij}\frac{\partial \Phi}{\partial \sigma_{ij}}\dot{\lambda}\,. \qquad (16)$$

In the above relations the gradient of the yield surface with respect to the stress state have been used several times and it can alternatively be expressed as

$$\frac{\partial \Phi}{\partial \sigma_{ij}} = \frac{\partial \Phi}{\partial \sigma_{e}}n_{ij} + \frac{1}{3}\frac{\partial \Phi}{\partial \sigma_{m}}\delta_{ij}, \qquad n_{ij} = \frac{3}{2}\frac{s_{ij}}{\sigma_{e}} \qquad (17)$$

where s_{ij} are the components of the deviatoric stress tensor of the aggregate.

3.2 Tangent modulus and an Euler forward integration procedure

To perform finite element calculations a stress update procedure has to be established and here the so called Euler forward, or explicit integration scheme, has been chosen due to that it is simpler to implement. The "forward" here means that the update of quantities when going from state n to state $n+1$ is determined from the known state at n. Each step (or load increment) is defined by the total strain increment $\Delta\varepsilon_{ij}$ that is to be reached at the end of the step, and is a known quantity in each load step. A version of equation (8) can then be used, to update the stress state, which relies on the elastic-plastic continuum tangent modulus D_{ijkl}^{ep}

$$\Delta\sigma_{ij} = D_{ijkl}^{ep}\Delta\varepsilon_{kl}\,. \qquad (18)$$

The rest of the update procedure, i.e. the evolution of internal variables and hardening, is then possible to calculate from the constitutive equations given in section 3.1, and will be summarized next.

The Euler forward update procedure from a load increment $n \to n+1$, given the (total) strain increment $\Delta\varepsilon_{ij}$, is summarized below:

1. Calculate elastic predictor stress: $\sigma_{ij}^{*} = \sigma_{ij}^{(n)} + \Delta\sigma_{ij}^{*}$, where $\Delta\sigma_{ij}^{*} = D_{ijkl}\Delta\varepsilon_{kl}$
2. Elastic or plastic step? Previous step was:
   a. Elastic: calculate $\Phi^{*} = \Phi\left(\sigma_{ij}^{*}, \bar{\sigma}^{(n)}, f^{(n)}\right)$. If > 0 then step is plastic go to point 4, else it is elastic and algorithm should go to point 3.
   b. Plastic: calculate $\dfrac{\partial\Phi^{(n)}}{\partial\sigma_{ij}}\Delta\sigma_{ij}^{*}$. If > 0 then step is plastic go to point 4, else it is elastic and algorithm should go to point 3.
3. Elastic step: standard linear elastic stress update $\sigma_{ij}^{(n+1)} = \sigma_{ij}^{(n)} + \Delta\sigma_{ij}^{*}$, $\bar{\sigma}^{(n+1)} = \bar{\sigma}^{(n)}$ and $f^{(n+1)} = f^{(n)}$.
4. Plastic step: Calculate elastic-plastic tangent $D_{ijkl}^{\mathrm{ep}\,(n)}$ (see below) used for new stress increment $\Delta\sigma_{ij} = D_{ijkl}^{\mathrm{ep}\,(n)}\Delta\varepsilon_{kl}$. Increments of plastic strain are $\Delta\varepsilon_{ij}^{p} = \Delta\varepsilon_{ij} - D_{ijkl}^{-1}\Delta\sigma_{kl}$ and increments of the internal variables are calculated as $\Delta\bar{\varepsilon} = \dfrac{\sigma_{ij}^{(n)}\Delta\varepsilon_{ij}^{p}}{\left(1-f^{(n)}\right)\bar{\sigma}^{(n)}}$, $\Delta f = \left(1-f^{(n)}\right)\left(\Delta\varepsilon_{kk}^{p} - 3\alpha\Delta\bar{\varepsilon}\right)$. Update the stress, strains and internal variables.

The Euler forward stress update depends, as stated above, on establishing the elastic-plastic tangent modulus as

$$D_{ijkl}^{\mathrm{ep}\,(n)} = D_{ijkl} - \frac{P_{ij}^{(n)}P_{kl}^{(n)}}{A^{(n)}}. \quad (19)$$

The tensor $P_{ij}^{(n)}$ is

$$P_{ij}^{(n)} = 2G\frac{\partial\Phi^{(n)}}{\partial\sigma_{e}}n_{ij}^{(n)} + K\frac{\partial\Phi^{(n)}}{\partial\sigma_{m}}\delta_{ij} \quad (20)$$

where G and K denote the elastic shear and bulk modulus, respectively, and the deviatoric direction tensor is given in equation (17). The scalar quantity $A^{(n)}$ is given by

$$A^{(n)} = H^{(n)} + P_{ij}^{(n)}\frac{\partial\Phi^{(n)}}{\partial\sigma_{ij}} \quad (21)$$

where $H^{(n)}$ can be calculated from equation (14) evaluated at state n.

3.3 A procedure for estimation of model parameters

The proposed model incorporates several parameters. The elasticity is governed by the Young's modulus E and Poisson's ratio ν. The porous plasticity description is dependent on initial porosity f_0 and the parameters q_1 and q_2. The dilatant matrix plasticity depends on the slope α and the strain hardening function $\bar{\sigma}(\bar{\varepsilon})$.

The tensile tests gave very consistent values on the Young's modulus so it is set to $E = 167$ GPa and based on values found in the literature Poisson's ration is set to $\nu = 0.275$ (reported values range from 0.25 to 0.3 and we settled for the average of this, see for instance Sundström (2010)). The initial porosity have been estimated from the micro structure analysis to be

$f_0 = 0.125$. This leaves three parameters and the matrix hardening to be estimated from the experiments. Here, as in the original GFS model as well as in the Gurson model, the parameter q_2 is set to unity, and will not be utilized in the calibration procedure. To determine the remaining two parameters (q_1,α) and the hardening function of the matrix material ($\bar{\sigma}(\bar{\varepsilon})$) a nonlinear optimization technique was used as will be explained next. The method consists of two nested procedures and is best explained by a schematic representation of the algorithm used as presented in Figure 3-2.

From the shear experiment determine $R_{p0.2}$ and back-extrapolate to a value for R_{p0}.

Set range of $q_1 = 1.00,\ 1.01, \ldots\ 2.25$ and limit $0 < \alpha < 0.1$

for each value of q_1 **do**

Set $\bar{\sigma}_0 = \dfrac{R_{p0}}{1 - q_1 f_0}$

Use nonlinear constrained minimization to determine which value of α that gives the best fit to experiments:

while error is not minimized **do**

Determine the matrix hardening:

for each load increment in the tensile experiment **do**

Explicit integration to solve the current load step and a non-linear search algorithm to find the slope h of the hardening curve $\Rightarrow \bar{\sigma}(\bar{\varepsilon})$.

end for

Use hardening function $\bar{\sigma}(\bar{\varepsilon})$ and current value of α to simulate the shear, $\tau_{23}(\gamma^{p}_{23})$, and compression, $\sigma_{33}(\varepsilon^{p}_{33})$, experiments.

Calculate root mean square error between simulation and experimental stress values for strains up to 10% plastic deformation.

end while

Save best fit parameters and error for specific value of q_1.

end for

Select the combination of $\{q_1,\ \alpha\}$ that has the lowest error.

Figure 3-2. Schematic representation of the nested minimization algorithm used to find the best fit values for the material parameters and the matrix hardening function.

Figure 3-3 shows the results from the minimization procedure in terms of mean relative error as a function of the value of q_1 and also the corresponding values of α. The best fit was found for $q_1 = 1.3283$ and $\alpha = 0.0648$.

The hardening relation is given as the flow stress of the matrix material $\bar{\sigma}$ as a function of accumulated equivalent deviatoric plastic strain in the matrix $\bar{\varepsilon}$. The hardening curve was extracted from the tensile experiment and could be determined experimentally up to about 13%

plastic strain. To extend the hardening relation to higher levels of strain the hardening curve above 11% was fitted to an exponential function as

$$\bar{\sigma}(\bar{\varepsilon}) = \bar{\sigma}_0 \left(1 + 1.994\,\bar{\varepsilon}^{0.3947}\right), \quad \bar{\varepsilon} > 0.11 \qquad (22)$$

where $\bar{\sigma}_0 = 320.4$ MPa. The hardening function is shown in Figure 3-4 where each point along the curve represents a table value that is later supplied as a user hardening function to the finite element simulations in Abaqus. It should be emphasized that equation (22) gives a poor fit to the experimentally determined hardening for an equivalent plastic strain in the range $0 < \bar{\varepsilon} < 0.10$.

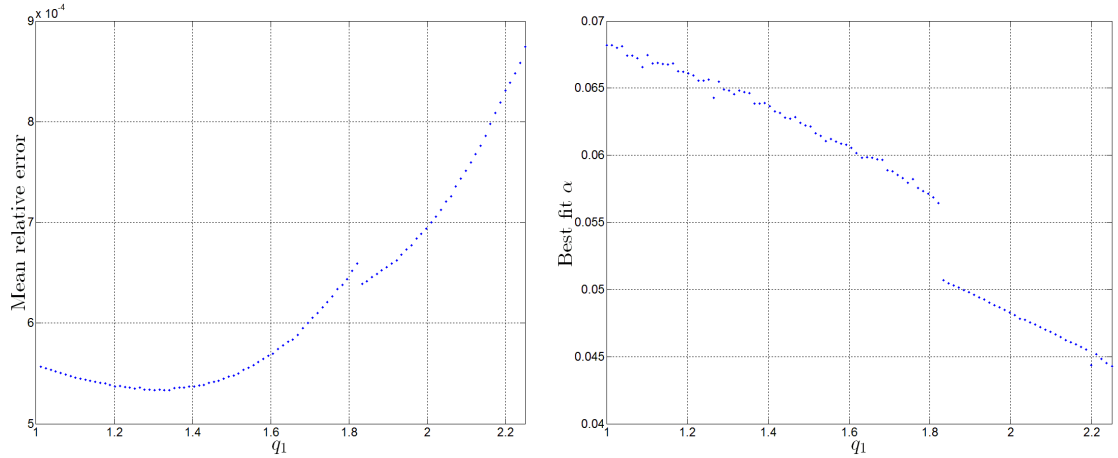

Figure 3-3. Results from the minimization algorithm. The discontinuity just above $q_1 = 1.8$ is due to a switch of which load case that gives the major contribution to the error function (shear or compression).

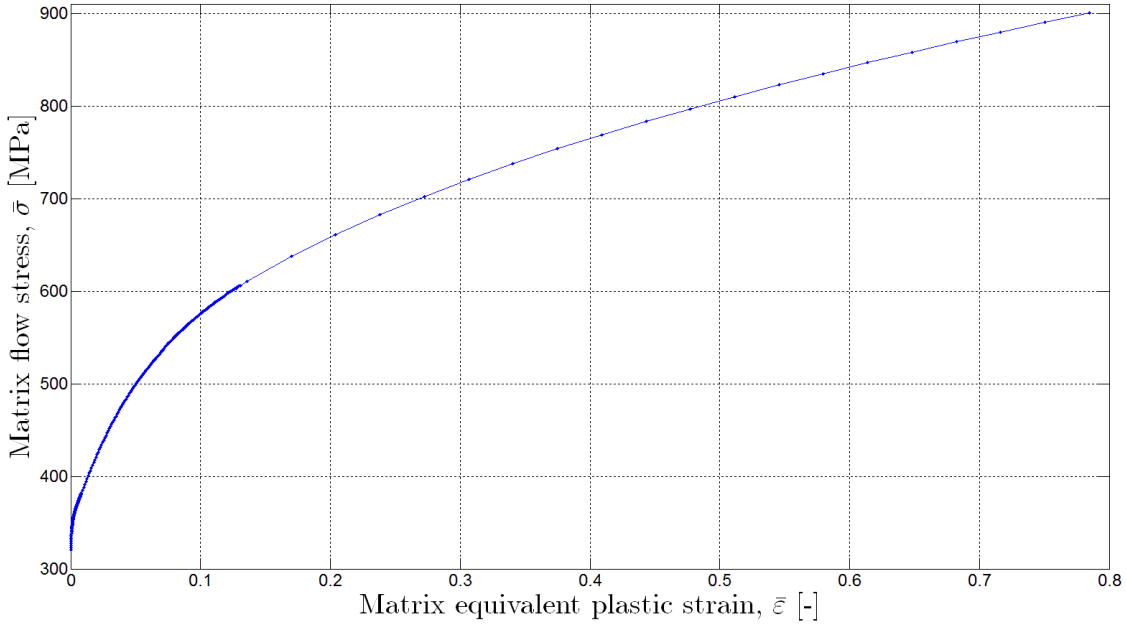

Figure 3-4. Matrix hardening relation for the full range of plastic strain – used in the subsequent FE simulations.

3.4 The best fit material parameters and comparison to experiments

A summary of the best fit material parameters is given in Table 3-1 below. With these parameters the three experiments with a homogeneous stress state, i.e. tension, compression and shear, can be simulated using the explicit integration algorithm but without the need for a finite element method implementation (this is the method that is used in the nonlinear optimization outlined above). A comparison between experiments and simulations is shown in Figure 3-5 where it should be emphasized that the model was optimized in the range of 0 to 0.1 in plastic strain.

Parameter	*Value*	*Description*
E	167 GPa	Young's modulus
ν	0.275	Poisson's ratio
$\bar{\sigma}_0$	320 MPa	Matrix yield stress
α	0.065	Matrix dilatancy slope
f_0	0.125	Initial porosity
q_1	1.33	Porosity parameter
q_2	1.00	Not used

Table 3-1. Best fit material parameters.

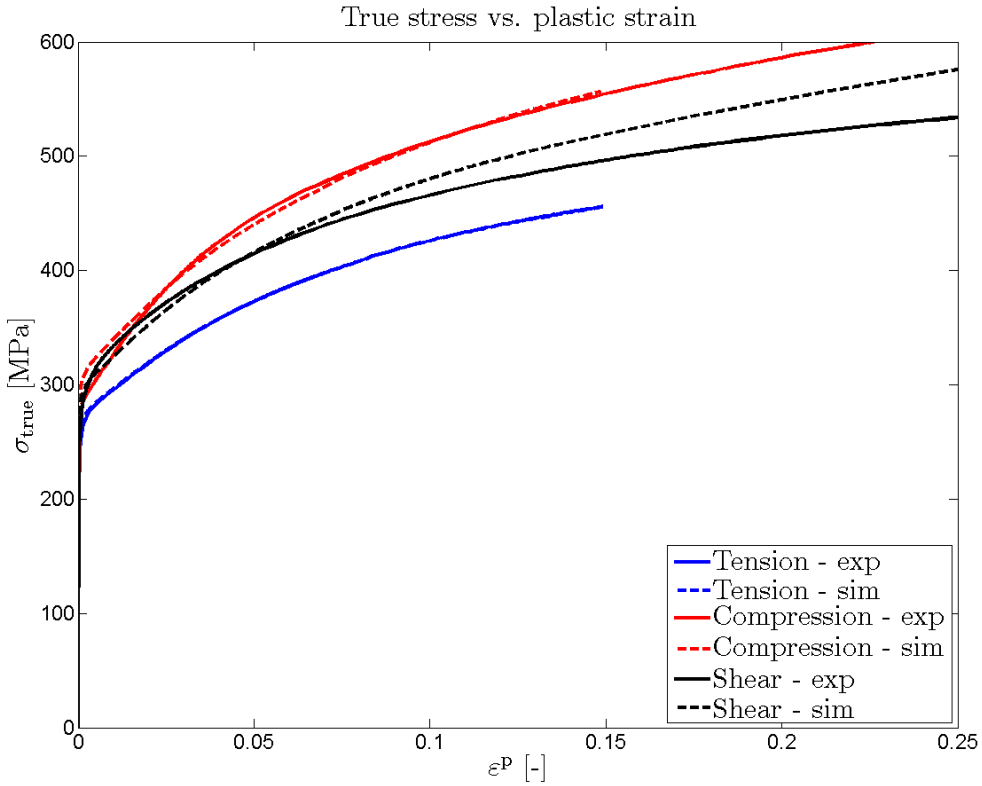

Figure 3-5. Comparison of experiments and simulation using the optimized material parameters for the three load cases with a homogeneous stress state.

From the simulations shown in Figure 3-5 the evolution of void volume fraction can also be plotted and is shown in Figure 3-6.

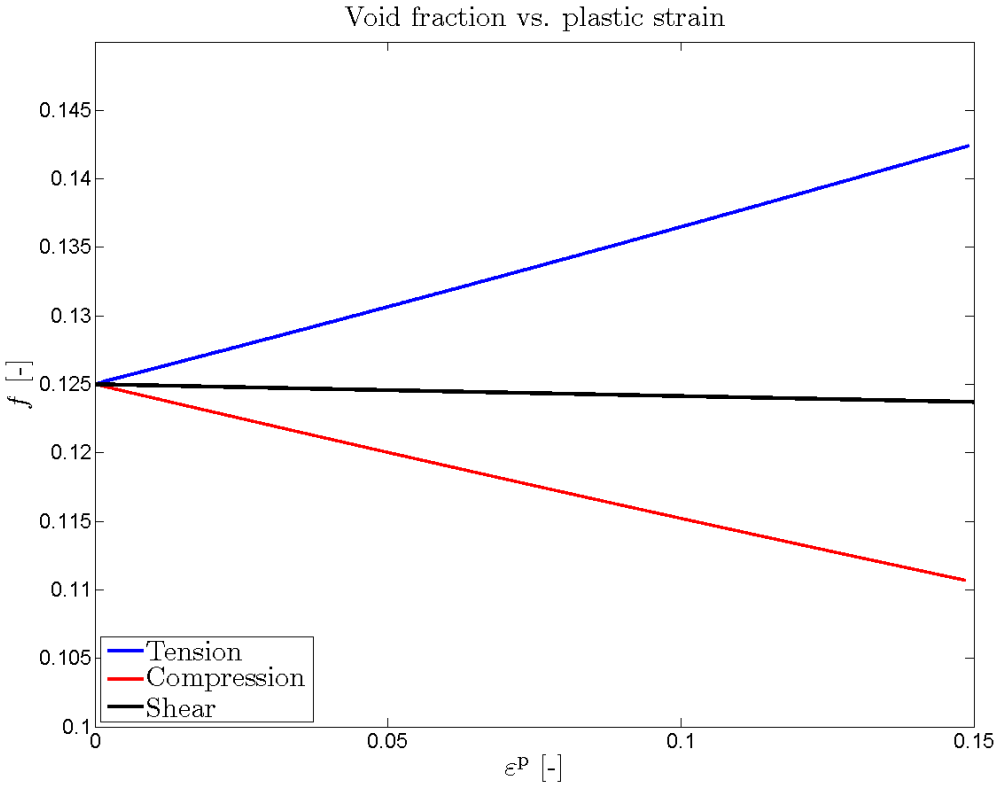

Figure 3-6. Evolution of void volume fraction for the three homogeneous stress states.

4 Comparison between experimental results and model predictions of test on notched round bar

4.1 FEM modeling

The GFS material model has been implemented in Abaqus Explicit as a user material subroutine for explicit integration (VUMAT). The two notched test specimens were modeled using axisymmetric elements and only half of the gauge length was modeled due to symmetry.

A constant velocity was prescribed on the top boundary and a symmetry condition was prescribed on the lower boundary. Since the explicit solver was used special care was taken to avoid initial shock waves through the material by prescribing an initial velocity on every node. The initial velocity was determined from the displacement field of a purely linear elastic solution performed before the elastic-plastic analysis.

4.2 FEM results and comparison with experiments

The FEM results were evaluated by outputting the reaction force and displacement of the top boundary, i.e. mimicking the data acquisition in the experiments. The FEM results are plotted in Figure 4-1 as thick dashed lines together with the experimental data. The colors corresponds to the two different specimen geometries where blue is for the shallow notch and red is for the notch with a smaller radius. As can be seen the result agree well with the experiments in terms of initial yield point and subsequent hardening, but of course cannot hope to capture the ductile failure since such a mechanism have not been implemented in the present model. It should here be emphasized that the model parameters were not fitted to these experiments at all so the FEM results are to be considered an actual prediction of the experiments.

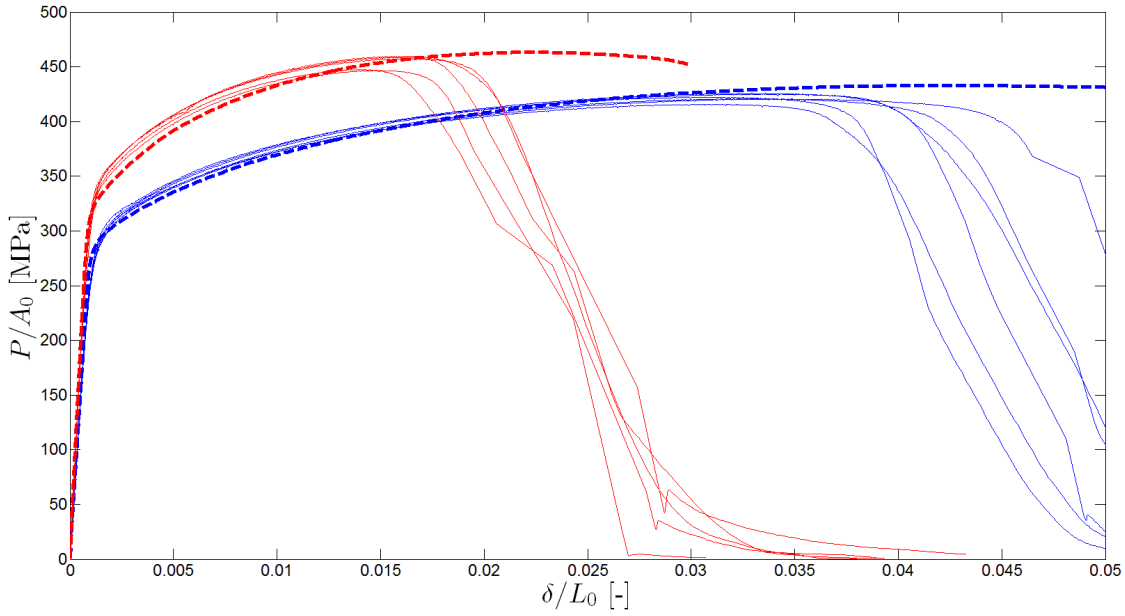

Figure 4-1. Comparison of notched tensile test curves to results predicted by the FEM model. Thick dashed lines represent the numerical model and thin solid lines are from the experiments. Blue curves are for the shallow notch and the red curves for the sharper notch. The abscissa gives the displacement of the gauge length and the ordinate is applied force normalized by the initial notch root area.

The evolution of void volume fraction for the two models was also tracked during the solution and is shown in Figure 4-2. The void volume fraction plotted is the nodal value at the node that sits exactly in the middle of the notch and experiences the largest void growth. In comparison to the results shown in Figure 4-1 it is interesting to note that for the shallow notch the experiments fail around 0.04 in normalized displacement and for the sharper notch this happen at about 0.0175. This corresponds to about the same value of void volume fraction (approximately 0.17) in Figure 4-2, thus hinting at 17% of voids being a candidate for a critical void volume fraction value. Another interesting observation that can be made is that the scatter in normalized displacement at the onset of failure noted in both the shallow and sharper notch experiments translates into critical void volume fractions in the range 16% to about 17.5%, which is a rather narrow variation.

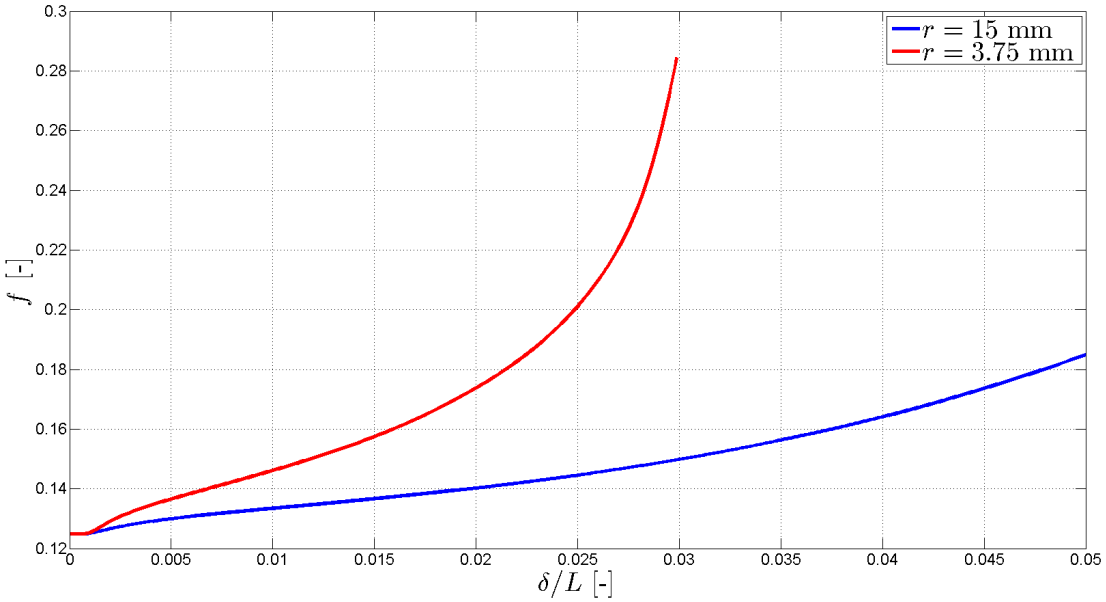

Figure 4-2. Evolution of void volume fraction in the center of the notch for both FE-models.

4.3 A comparison to other candidate models

As a comparison the two types of notched round bar specimens were also analyzed by use of a standard J_2 (or Mises) material and a Gurson–Tvergaard (GT) material. The isotropic hardening function for the Mises material was directly taken from the uniaxial stress-strain response from the so called "Master curve" from the tests on the smooth round bar specimens. To achieve the response of a Gurson–Tvergaard material, $\alpha = 0$ in the GFS-model, while keeping all the other material parameters unchanged. This means that the GFS and the GT material, respectively, would yield the same response in the torsion test in pure shear, cf. Figure 3-1. The results from these analyses are plotted in Figure 4-3 in the same manner as in Figure 4-1. Note, that the analysis based on the Mises material and the GT material, respectively, severely overestimate the force level.

Calculations based on a J_2 theory may be justified in cases where the stress state is fairly homogeneous and where the plastic flow properties is determined for the particular stress state in question. Thus, adopting plastic flow properties from compression tests in analysis on structures primarily loaded in tension may lead to a significant over prediction of load levels. Also, due to the mechanics of a porous material the aggregate is expected to deformation-harden more in compression than in tension. In conclusion the plastic behavior of the canister insert NCI is too complicated to be accurately described by a simple deformation type plasticity formulation as can be found in for example Minnebo and Vokal (2007) and even a more complicated GT-type model will not suffice according to the results obtained here.

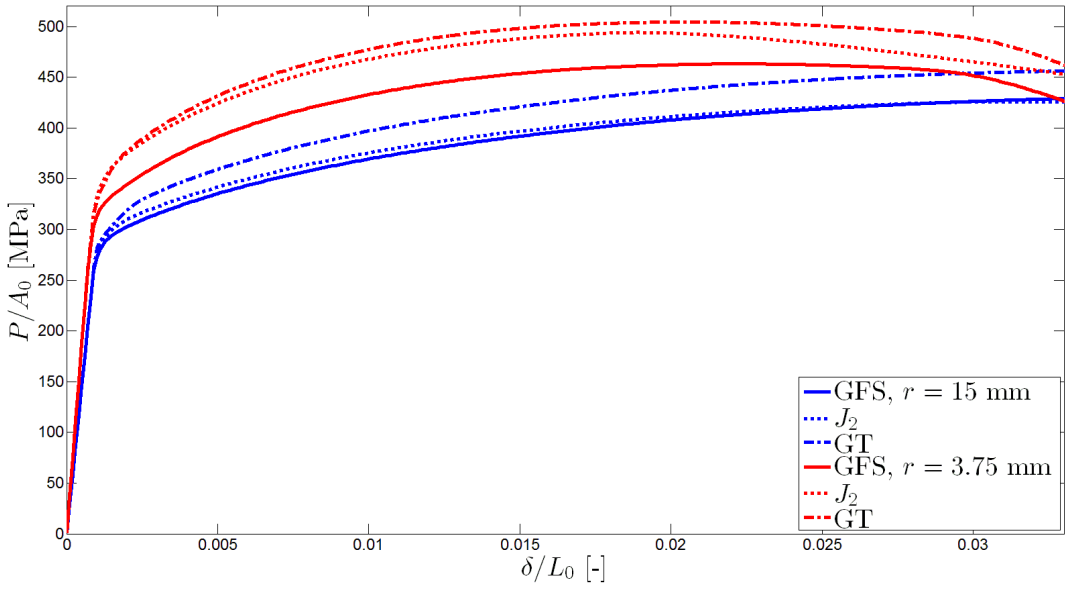

Figure 4-3. Predictions of the notched round bar tests where the proposed model (GFS) is compared to a standard J_2 plasticity model and the Gurson-Tvergaard model.

5 Fractographic examination

The relative strong influence of hydrostatic stress on the yield behavior and ductile failure observed in the cast iron is to a large degree due to the relatively large void volume fraction of voids that nucleate and grow to coalescence. The primary nucleation sites of these voids are at or rather around the spherical graphite nodules in the cast iron. Information about this process can be found from studying fracture surfaces from the different tests. Here, a limited fractographic examination will be presented of some of the fracture surfaces from tests carried out in pure tension and shear. For comparison purposes, observations from a fracture surface pertaining to a tensile test conducted under liquid nitrogen temperature conditions will also be discussed.

5.1 Uniaxial tension specimens

The fracture surface shown in Figure 5-1, belong to Specimen 17250 and is tested in uniaxial tension. The strain to failure was about 0.19 in this test. Note that Figure 5-1(b) is a close-up of the dashed rectangular area shown in Figure 5-1(a), and that Figure 5-1(c) is a close-up of the dashed rectangular area shown in Figure 5-1(b). It can be observed that the fracture surface is filled with dimples. About half of the dimples contain graphite nodules, and it is anticipated that the other half is stuck on the opposite fracture surface. The fractographs clearly suggests that voids nucleate by graphite nodules that debond from the ferrite matrix. Final failure occurs when these voids essentially grow to impingement as seen by the very thin ridges that separates the dimples on the fracture surface. It can also be observed that coalescence has been assisted by a limited amount of secondary voids, see Figure 5-1(b,c). Even though stress triaxiality is as low as about 0.33, the voids seem to have grown in an essential spherical manner, and at the onset and progression of coalescence, growth appears to be localized to the equatorial plane until the voids impinge on each other.

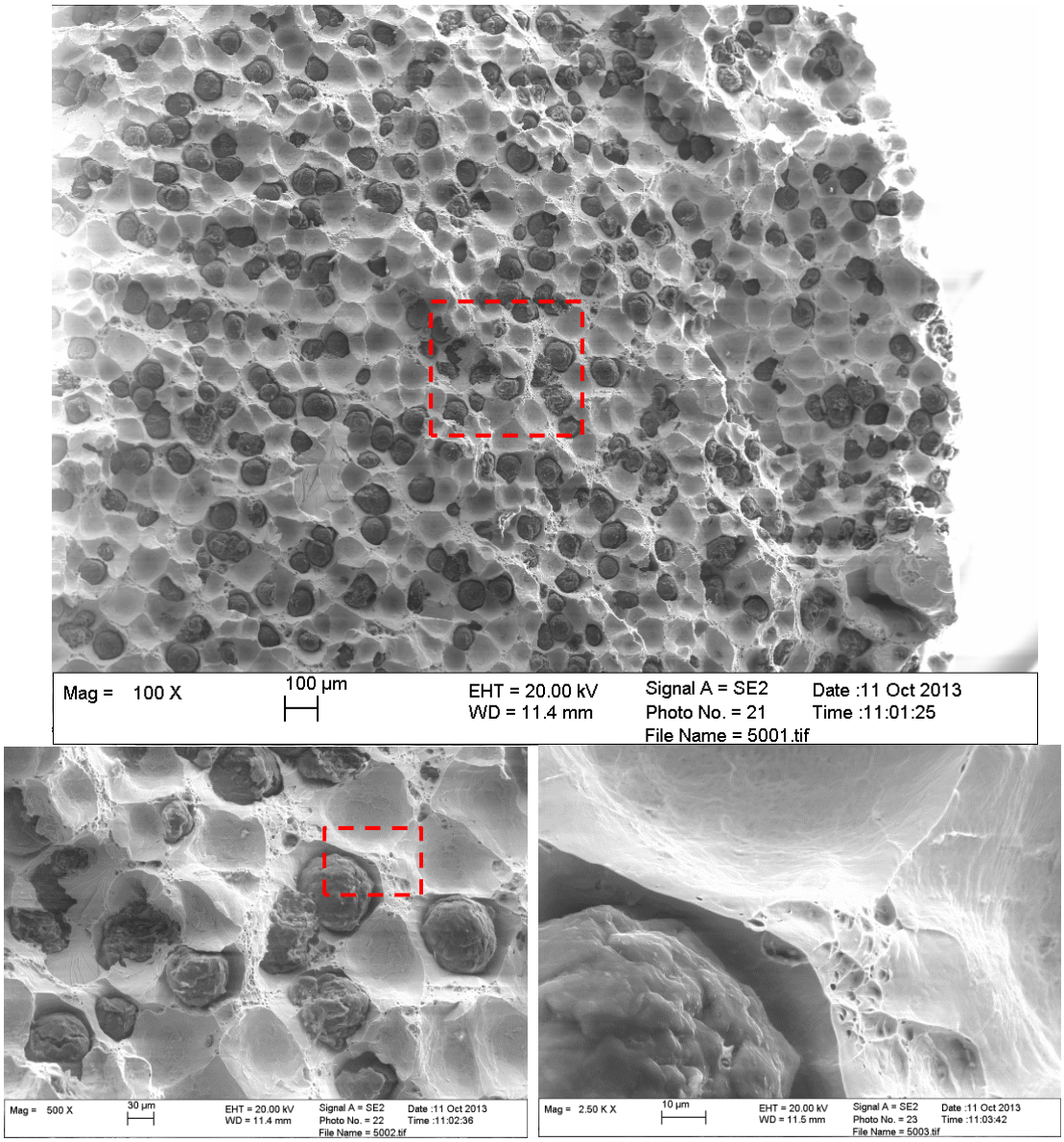

Figure 5-1. Fracture surface taken from Specimen 17250 tested in uniaxial tension showing an overall picture in (a) and close-ups in (b) and (c). The scale in each picture is indicated by the scale bar.

5.2 Pure shear specimen

The appearance of the fracture surfaces shown in Figure 5-2, belonging to Specimen 17306 tested in pure shear, are significantly different from the fracture surface shown in Figure 5-1. Here, the fracture surface is characterized by voids that flattened and rotate until the onset of coalescence. Note that the graphite nodules have deformed severely and to some extent deboned from the ferrite matrix, but they are still contained in the flattened voids. From the close-up pictures in Figure 5-2(b,c), it can be seen that final link-up of the flattened and rotated voids is assisted by a second populations of voids. This second population of voids have after nucleation, undergone much the same type of growth involving flattening and rotation as the primary voids have.

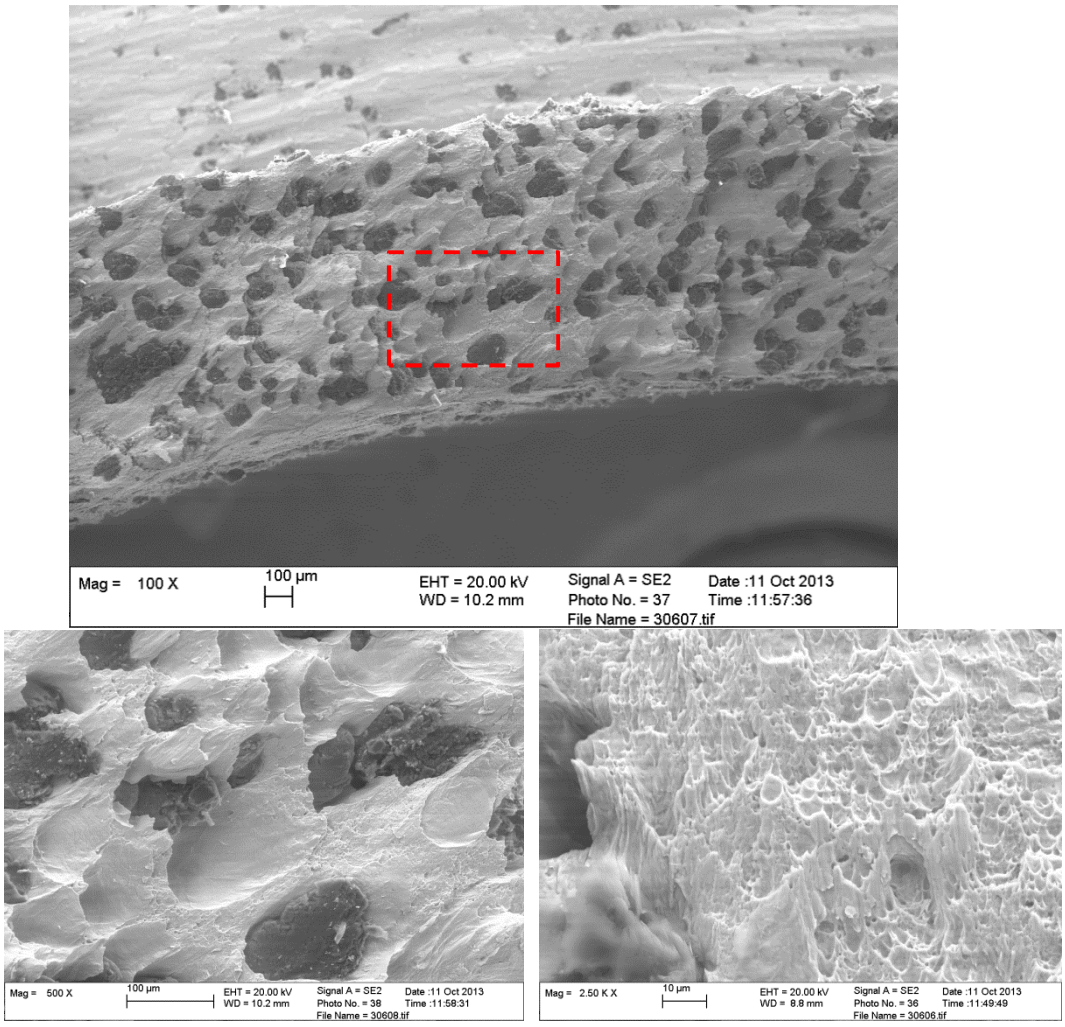

Figure 5-2. Fracture surface taken from Specimen 17306 tested in pure shear showing an overall picture in (a) and close-ups in (b) and (c). The scale in each picture is indicated by the scale bar.

5.3 Evidence of casting defects

In one of the uniaxial tests, Specimen 17248, the strain to final failure was significantly lower. Here, the failure strain was less than 0.04 as opposed to the second lowest value being more than twice as high. Figure 5-3(a), with a close-up of the rectangular dashed region shown in Figure 5-3(b), shows the fracture surface of Specimen 17248. The picture is taken from the part of the surface that is believed to comprise the cause of the premature occurrence of fracture. By careful inspection of the surface it can be concluded that the plane of fracture contains several casting defects (pores), which becomes evident by the close-up in Figure 5-3(b), notice the smooth surface. Here, the casting defect may be seen as a number of voids that already from the outset have coalesced into one large void or volumetric defect. Thus, as the initial void volume fraction was high locally, a macro crack initiated and started to grow in a stable manner when the macro strain reached a value of almost 0.04. To propagate the crack through the cross-section of the smooth round bar specimen, an additional strain of about 0.015 needed to be applied. Hence, the variation in failure strain seen in the tests presented above depends not only on a spatial variation of graphite nodules and their individual sizes; it is also strongly affected by casting defects. However, it should be pointed out that neither the variation of the graphite nodules in size and space, nor the presence of casting defects seem to affect the overall plastic flow behavior of the material at large.

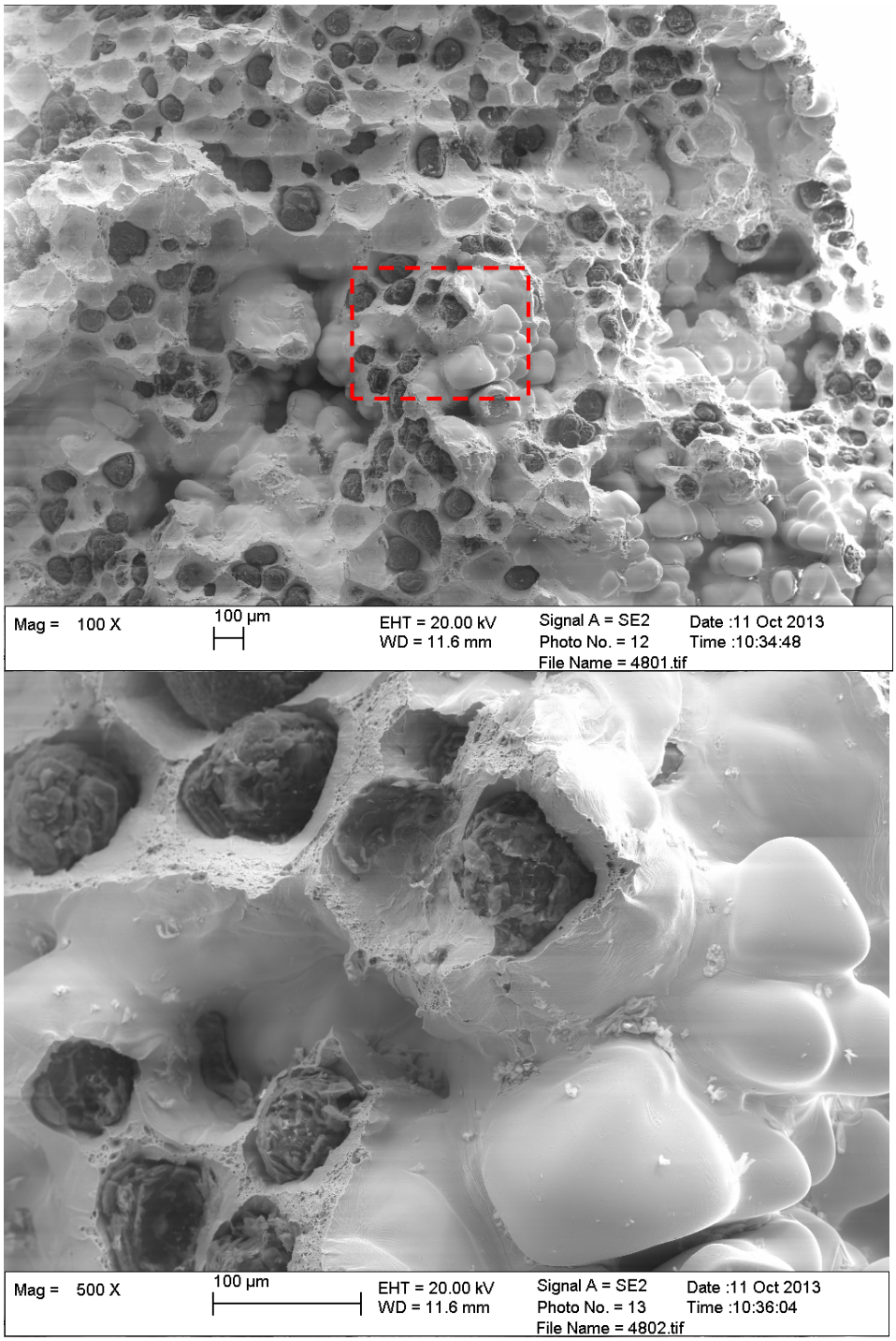

Figure 5-3. Fracture surface taken from Specimen 17248 tested in uniaxial tension showing an overall picture in (a) and close-ups in (b). The scale in each picture is indicated by the scale bar. The failure in the test was triggered by casting defects and therefore failure occurred at low strains.

5.4 Liquid nitrogen temperature fracture surface

For comparison purposes, a test was performed under liquid nitrogen temperature conditions, i.e. at $-196°$ C. The fractograph of this test is displayed in Figure 5-4. As expected, the fracture surface is covered by cleavage facets that follow the dominating cleavage planes of the BCC lattice of the ferrite matrix. These cleavage planes are especially clear in the close-up pictures in Figure 5-4(b,c). In the latter pictures another interesting observation may be done, where it can

be seen that also some of the graphite nodules have fractured in two pieces rather than deboned from the matrix, e.g. see the nodule in the upper part of Figure 5-4(b). Finally, some regions containing dimples are visible in the upper part of Figure 5-4(a), and shown at a higher magnification in Figure 5-4(d). However, cleavage facets were not found on fracture surfaces from specimens tested at room temperature.

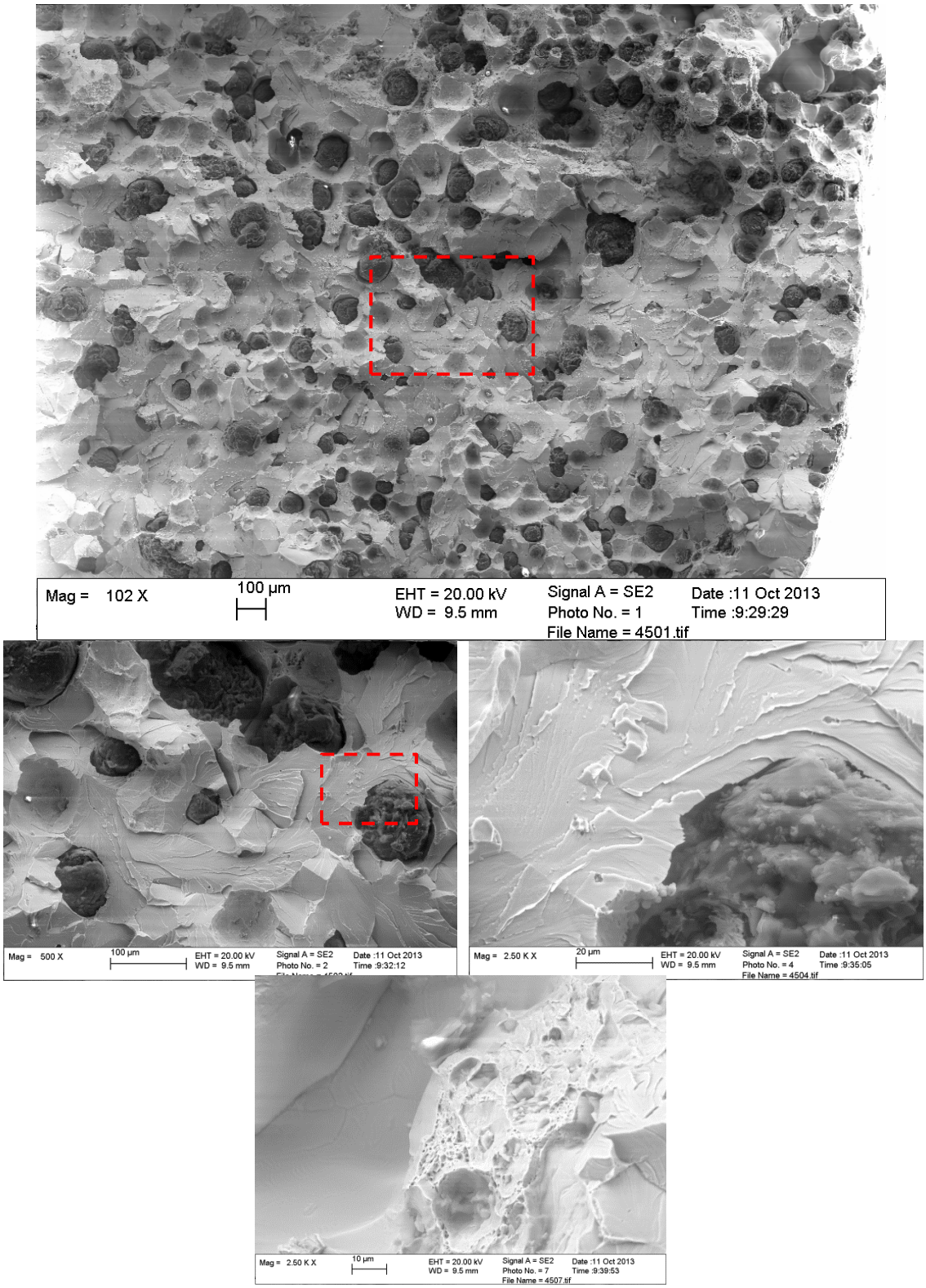

Figure 5-4. Fracture surface taken from Specimen 17345 tested in uniaxial tension at liquid nitrogen temperature. An overall picture of the fractured surface is displayed in (a) with subsequent close-ups shown in (b), (c). In (d) evidence of a small amount of dimple rupture can be observed.

6 Conclusions

An investigation of the nodular cast iron material to be used in the copper canister inserts for spent nuclear fuel has been carried out. With the purpose of characterizing the material under stress state conditions typical for the application, a series of tests were executed in the stress triaxiality regime -0.33 to 0.67. This was accomplished by tests in uniaxial compression, in pure shear, in uniaxial tension and in tests on two different types of notched round bars. The latter two were included for verification purposes. Guided by the outcome from the tests, the model for a porous plastic solid based on a matrix material with a Drucker-Prager yield criterion proposed by Guo et al. (2008) was employed. The results from tests in uniaxial compression, pure shear and uniaxial tension were used to calibrate the material parameters. The model was verified by comparing model predictions for the notched bar tests with the corresponding experimental results. As the agreement was very good, it can be concluded that the model chosen appear to capture the important features of the elastic-plastic response in a range of stress triaxiality of interest for the application. The primary cause of the strong influence of the mean stress on the plastic response is due to the presence of graphite nodules in the cast iron material. From several independent investigations of the microstructure, the average volume fraction of graphite nodules came out as 12.5%. These investigations also revealed that the concentration of graphite nodules exhibited a substantial variation in space, and also in size. The influence of these variations on the plastic response was minimal. However, the relatively large scatter in the strain to failure can to some extent be associated with these variations.

7 References

Bao Y, Wierzbicki T, 2004. On fracture locus in the equivalent strain and stress triaxiality space. International Journal of Mechanical Sciences 46, 81–98.

Benseddiq N, Imad A, 2008. A ductile fracture analysis using a local damage model. International Journal of Pressure Vessels and Piping 85, 219–227.

Benzerga AA, Leblond J-B, 2010. Ductile Fracture by Void Growth to Coalescence. Advances in Applied Mechanics 44, 169–305.

Berdin C, Dong MJ, Prioul C, 2001. Local approach of damage and fracture toughness for nodular cast iron. Engineering Fracture Mechanics 68, 1107–1117.

Bonora N, Ruggiero A, 2005. Micromechanical modeling of ductile cast iron incorporating damage. Part I: Ferritic ductile cast iron. International Journal of Solids and Structures 42, 1401–1424.

Brocks W, Hau S, Steglich D, 1996. Micromechanical Modelling of the Damage and Toughness Behaviour of Nodular Cast Iron Materials. Journal de Physique IV 6, 43–52.

Chen ZM, Mrovec M, Gumbsch P, 2013. Atomistic aspects of $\frac{1}{2}\langle 111 \rangle$ screw dislocation behavior in α -iron and the derivation of microscopic yield criterion. Modelling and Simulation in Materials Science and Engineering 21, 1–18.

Dao M, Lee BJ, Asaro RJ, 1996. Non-Schmid effects on the behavior pf polycrystals-with applications to Ni_3Al. Metallurgical and Materials Transactions 27A, 81–99.

Faleskog J, Gao X, Fong Shih C, 1998. Cell model for nonlinear fracture analysis – I. Micromechanics calibration. International Journal of Fracture 89, 355–373.

Friel JJ, Grande JC, Hetzner D, 2000. Practical Guide to Image Analysis. *ASM International*, Materials Park, OH, USA.

Ghahremaninezhad A, Ravi-Chandar K, 2012. Deformation and failure in nodular cast iron. *Acta Materialia* 60, 2359–2368.

Guo TF, Faleskog J, Shih CF, 2008. Continuum modeling of a porous solid with pressure-sensitive dilatant matrix. Journal of the Mechanics and Physics of Solids 56, 2188–2212.

Gurson AL, 1977. Continuum theory of ductile rapture by void nucleation and growth: part I - yield criteria and flow rules for porous ductile media. Journal of Engineering Materials and Technology 99, 2–15.

Jenkins LR, Forrest RD, 1990. Ductile Iron, Properties and Selections: Irons, Steels, and High-Performance Alloys. In: ASM Handbook, Vol 1, ASM International, 33–55.

Martínez RA, 2010. Fracture surfaces and the associated failure mechanisms in ductile iron with different matrices and load bearing. Engineering Fracture Mechanics 77, 2749–2762.

Minnebo P, Vokál V, 2007. Compression Properties of Six KBS-3 Canister Inserts. JRC Scientific and Technical Report 41361, Joint Research Centre, Institute for Energy, The Netherlands.

Needleman A, 1985. On finite element formulations for large elastic-plastic deformations. Computers & Structures 20, 247–257.

Nilsson K-F, Vokál V, 2009. Analysis of ductile cast iron tensile tests to relate ductility variation to casting defects and material microstructure. Material Science and Engineering A 502, 54–63.

Pastor F, Kondo D, Pastor J, 2013. 3D-formulations of limit analysis methods for porous pressure-sensitive materials. International Journal for Numerical Methods in Engineering 95, 847–870.

Shi YW, Cheng JX, Chen BY, 1992. The effect of stress state on the ductility and the critical extent of void growth in nodular cast iron. Material Science and Engineering A149, 195–202.

Steglich D, Brocks W, 1997. Micromechanical modelling of the behaviour of ductile materials including particles. Computational Material Science 9, 7–17.

Steglich D, Brocks W, 1998. Micromechanical modelling of damage and fracture of ductile materials. Fatigue and Fracture of Engineering Materials and Structures 21, 1175–1188.

Sundström B (Editor), 2010. Handbok och formelsamling i Hållfasthetslära" 7:e utgåvan. Institutionen för Hållfasthetslära KTH, Stockholm.

Tjahjanto D, 2008. Micromechanical modeling and simulations of transformation-induced plasticity in multiphase carbon steels. PhD-thesis, Delft University of Technology, Delft, The Netherlands.

Tvergaard V, 1981. Influence of voids on shear band instabilities under plane strain conditions. International Journal of Fracture 17, 389–407.

Tvergaard V, 1982. Ductile fracture by cavity nucleation between larger voids. Journal of the Mechanics and Physics of Solids 30, 265–286.

Tvergaard V, 1990. Material Failure by Void Growth to Coalescence". Advances in Applied Mechanics 27, 83–151.

Vitek V, Mrovec M, Gröger R, Bassani JL, Racherla V, Yin L, 2004. Effects of non-glide stresses on the plastic flow of single and polycrystals of molybdenum". Material Science and Engineering A389, 138–142.

Zhang KS, Bai JB, Francois D, 1999. Ductile fracture of materials with high void volume fraction. International Journal of Solids and Structures 36, 3407–3425.

Unpublished documents

SKBdoc id, version	Title	Issuer, year
1094762, ver 1.0	Materialprovning av segjärnsinsats I53. (In Swedish.)	SweCast AB, 2007
1206724, ver 1.0	Materialprovning av segjärnsinsats I53 (Mitten/Botten). (In Swedish.)	SweCast AB, 2007
1401573, ver 2.0	Strukturundersökning vidgjutna ämnen I53-I57. (In Swedish.)	Swerea SweCast AB, 2013